Building a Young Mountain Range: Insight into the Along-Strike Exhumation History of the Greater Caucasus Mountains from Detrital Zircon (U-Th)/He Thermochronology and 10Be Erosion Rates

Adam Matthew Forte[1,1,1,1], Kate R Gutterman[1,1,1,1], Matthijs C van Soest[2,2,2,2], and Kerry Gallagher[3,3,3,3]

[1]Louisiana State University
[2]Arizona State University
[3]Universite de Rennes 1

November 30, 2022

Abstract

The Greater Caucasus (GC) Mountains within the central Arabia-Eurasia collision zone, are an archetypal example of a young collisional orogen. However, the mechanisms driving rock uplift and forming the topography of the range are controversial, with recent provocative suggestions that uplift of the western GC is strongly influenced by an isostatic response to slab detachment, whereas the eastern half has grown through shortening and crustal thickening. Testing this hypothesis is challenging because records of exhumation rates mostly come from the western GC, where slab detachment may have occurred. To address this, we report 623 new, paired zircon U-Pb and (U-Th)/He ages from 7 different modern river sediments, spanning a ~400 km long gap in bedrock thermochronometer data. We synthesize these with prior bedrock thermochronometer data, recent catchment averaged 10Be cosmogenic exhumation rates, topographic analyses, structural observations, and plate reconstructions to evaluate the mechanisms growing the GC topography. We find no evidence of major differences in rates or timing of onset of cooling or total amounts of exhumation across the possible slab edge, inconsistent with previous suggestions of heterogeneous drivers for exhumation along-strike. Comparison of exhumation across timescales highlight a potential acceleration, but one that appears to suggest a consistent northward shift of the locus of more rapid exhumation. Integration of these new datasets with simple models of orogenic growth suggest that the gross topography of the GC is explainable with traditional models of accretion, thickening, and uplift and does not require any additional slab-related mechanisms.

Hosted file

`rev_gc_detrital_supplement_v4.docx` available at https://authorea.com/users/560667/articles/608574-building-a-young-mountain-range-insight-into-the-along-strike-exhumation-history-of-the-greater-caucasus-mountains-from-detrital-zircon-u-th-he-thermochronology-and-10be-erosion-rates

Building a Young Mountain Range: Insight into the Growth of the Greater Caucasus Mountains from Detrital Zircon (U-Th)/He Thermochronology and ^{10}Be Erosion Rates

Adam M. Forte[1], Kate R. Gutterman[1†], Matthijs C. Van Soest[2], and Kerry Gallagher[3]

[1]Department of Geology & Geophysics, Louisiana State University, Baton Rouge, Louisiana, USA.

[2]School of Earth and Space Exploration, Arizona State University, Tempe, Arizona, USA.

[3]Géosciences Rennes/OSUR, University of Rennes, Rennes, France.

Corresponding author: Adam M. Forte (aforte8@lsu.edu)

†Now at Chevron.

Key Points:

- New detrital thermochronology fills 400 km long gap in bedrock data that hindered interpretation of exhumation mechanisms within the Greater Caucasus.
- Synthesis of new and existing thermochronology data imply similar magnitudes and timing of exhumation along-strike in the Greater Caucasus.
- Comparison of exhumation rates with long-term estimates of convergence do not require isostatic uplift from slab detachment.

Abstract

The Greater Caucasus (GC) Mountains within the central Arabia-Eurasia collision zone, are an archetypal example of a young collisional orogen. However, the mechanisms driving rock uplift and forming the topography of the range are controversial, with recent provocative suggestions that uplift of the western GC is strongly influenced by an isostatic response to slab detachment, whereas the eastern half has grown through shortening and crustal thickening. Testing this hypothesis is challenging because records of exhumation rates mostly come from the western GC, where slab detachment may have occurred. To address this data gap, we report 623 new, paired zircon U-Pb and (U-Th)/He ages from 7 different modern river sediments, spanning a ~400 km long gap in bedrock thermochronometer data. We synthesize these with prior bedrock thermochronometer data, recent catchment averaged ^{10}Be cosmogenic exhumation rates, topographic analyses, structural observations, and plate reconstructions to evaluate the mechanisms growing the GC topography. We find no evidence of major differences in rates, timing of onset of cooling, or total amounts of exhumation across the possible slab edge, inconsistent with previous suggestions of heterogeneous drivers for exhumation along-strike. Comparison of exhumation across timescales highlight a potential acceleration, but one that appears to suggest a consistent northward shift of the locus of more rapid exhumation. Integration of these new datasets with simple models of orogenic growth suggest that the gross topography of the GC is explainable with traditional models of accretion, thickening, and uplift and does not require any additional slab-related mechanisms.

Plain Language Summary

The transition from subduction to building of mountain ranges is a fundamental process shaping the rock record, but our understanding of this process is limited by few well preserved examples. One where this transition is preserved is in the Greater Caucasus Mountains, but the first order drivers of rock uplift and growth of topography remain controversial. Here, it seems the eastern half of the range grew by shortening and thickening of the crust, but uplift of the western half may be driven by removal of a subducted slab. Importantly, direct records of the rate of erosion or exhumation are largely absent in the eastern range. Here we report new data, derived from zircon grains extracted from modern sediments which span the length of the range. Integrating these with prior analyses of cooling rates derived from minerals from in-situ bedrock

samples, we find no meaningful change in the rates at which rocks have uplifted or the total magnitude of rock exhumation along the whole range. Consideration of these new data with records of millennial scale exhumation rates and total amounts of plate motion imply that the evolution of growth of the Greater Caucasus is well explained by shortening and thickening.

1 Introduction

The growth of collisional mountain ranges necessarily implies a transition from subduction to collision, but the details of this process, and the mechanisms important in the early development of orogenic topography, are often obscured in mature or ancient orogenic systems, with much of our insight instead gained from modelling (e.g., Beaumont et al., 1996; Ellis et al., 1999; Ellis & Beaumont, 1999; Jamieson & Beaumont, 2013; Pfiffner et al., 2000; Vanderhaeghe, 2012; Vanderhaeghe & Duchene, 2010; Willett et al., 2001). Alternatively, this critical transition can be studied directly in a variety of places where this process is still ongoing or has occurred very recently (e.g., Eberhart-Phillips et al., 2006; Harris et al., 2009; Kao et al., 2000; Lester et al., 2013; Regard et al., 2004, 2010; Reyners & Cowan, 1993; Tate et al., 2015). Among these locations, the Greater Caucasus (GC) Mountains are unique in that they (1) are one of the few such environments that is almost completely onshore, providing unprecedented access to the entirety of the system, (2) involve continent-continent collision as opposed to arc-continent collision, (3) are proceeding at a modest rate both in terms of convergence and rock uplift, and (4) are primarily eroded by fluvial erosion in the absence of extreme weather events, i.e., typhoons or seasonal monsoons (e.g., Adamia, Zakariadze, et al., 2011; Avdeev & Niemi, 2011; Forte et al., 2014, 2016, 2022; Reilinger et al., 2006; Vasey et al., 2020; Vincent et al., 2011, 2020).

The GC represents the main locus of shortening within the central Arabia-Eurasia collision zone (e.g., Allen et al., 2004; Jackson, 1992; Reilinger et al., 2006), and has long been considered an archetypal example of a young collisional orogen (e.g., Philip et al., 1989). In the GC, thermochronology results from the center of the range suggest rapid exhumation, and presumably the generation of significant topography, beginning during the Plio-Pleistocene (e.g., Avdeev & Niemi, 2011). However, the exact timing and style of exhumation within the GC has proven controversial, calling into question both whether it is in fact a particularly young orogen and whether the dominant mechanisms driving development of the range's topography is typical of collisional ranges. Specifically, thermochronology results from different parts of the range than those sampled by Avdeev & Niemi (2011), along with sedimentological evidence, suggest that the range was built via slower and more steady exhumation since the late Eocene to Oligocene (e.g., Vincent et al., 2007, 2011) and had achieved significant, km-scale, topographic growth by this time (Vincent et al., 2016). These two different timelines of exhumation and topographic development of the range are bound up with disagreements with respect to how shortening is accommodated within the GC and the nature of the pre-collisional structural and basin architecture of the region, which fundamentally tie to when collisional related exhumation began (e.g., Cowgill et al., 2016, 2018; Vincent et al., 2016, 2018). Much of the controversy in terms of timing and rate of exhumation was contrived in the sense that samples suggestive of gradual slow cooling came from the low-relief flanks of the range, whereas those indicating more rapid and recent cooling came from the high-relief core. Thus, neither dataset needs to be wrong as they were comparing portions of the range reflecting different aspects of its tectonic and exhumation history (Forte et al., 2016). More recently, new sampling and thermal modelling has mostly resolved the controversy, finding a consistent pattern of rapid (~ 1 km/Myr) and recent (< 5-10 Ma) exhumation in the core of the range, with older and slower exhumation along the flanks (Vincent et al., 2020).

However, what has emerged from recent work in the GC is a complex view of a mountain range in which exhumation and topographic growth along-strike may be driven by decidedly different geodynamic and tectonic processes (Vincent et al., 2020). Adding to the complication, the gross topography of the GC, which is characterized by relative uniformity, seemed at odds with modern climatic and tectonic forcing (Forte et al., 2016). In detail, isostatic response to the detachment of a subducted slab beneath the western GC (Mumladze et al., 2015), may contribute some (Forte et al., 2016) to nearly all of the observed rapid exhumation within the western GC (Vincent et al., 2020). In contrast, clear evidence of a still extant, attached slab in the eastern GC (e.g., Gunnels et al., 2020; Mellors et al., 2012; Mumladze et al., 2015; Skolbeltsyn et al., 2014) seems compatible with shortening, accretion, and crustal thickening as the primary drivers of exhumation and topographic growth (Forte et al., 2016). However, the operation of differing dominant exhumation mechanisms along-strike are challenging to test because the vast majority of published low-temperature thermochronology data lie within the region that may have experienced slab detachment (e.g., Avdeev & Niemi, 2011; Král & Gurbanov, 1996; Vasey et al., 2020; Vincent et al., 2011, 2020). Qualitative evaluation of different exhumation rates or mechanisms along-strike from the topography is also challenging because of the apparent low sensitivity of the gross topography of the range to tectonic forcing (Forte et al., 2016, 2022).

A critical appraisal of the hypothesis of a variation in primary exhumation mechanism, and thus dominant mechanism by which the topography of the GC has grown, requires data in the area east of the hypothesized subducted slab edge. However in detail, there is a nearly 400 km wide gap in published low-temperature thermochronology data (Figure 1). This data gap in part exists because of the lack of suitable lithologies for bedrock samples throughout much of the central and eastern range, which is dominated by flysch (Adamia, Zakariadze, et al., 2011; Forte et al., 2014; Saintot et al., 2006). Here we in part fill this thermochronologic gap with a suite of new detrital zircon (U-Th)/He data from modern river sands which overcome the relatively low yields of suitable thermochronometers from in-situ bedrock samples in this section of the range. In order to consider as complete a history of the development of the topography of the GC and evaluate whether the range is well explained by traditional models of orogenic growth or if it requires extra contributions from slab-related processes, we then integrate these new detrital thermochronologic data with a synthesis of published low-temperature bedrock thermochronology data (Avdeev, 2011; Avdeev & Niemi, 2011; Bochud, 2011; Král & Gurbanov, 1996; Tye, 2019; Vasey et al., 2020; Vincent et al., 2011, 2020), recent structural observations (Trexler et al., 2022; Tye, 2019), regional plate reconstructions (van der Boon et al., 2018; van Hinsbergen et al., 2019), topographic analysis, and millennial scale exhumation rates from catchment averaged, cosmogenic ^{10}Be in quartz (Forte et al., 2022). We use this synthesis to both evaluate models suggestive of differing primary drivers for exhumation along-strike and more generally explore the record of exhumation and topographic growth in the GC as the range transitioned from subduction to collision.

2 Background

2.1 Tectonic setting

The GC has likely been the main locus of shortening within the central Arabia-Eurasia collision zone since at least ~5 Ma. This timing coincides with a regional plate reorganization (e.g., Allen et al., 2004; Axen et al., 2001), though as highlighted by Vincent et al., (2020), the exact timing of this reorganization may be diachronous throughout the collision (e.g., Ballato et al., 2011; Barber et al., 2018; Gavillot et al., 2010; Madanipour et al., 2017; Mouthereau, 2011; Rezaeian et al., 2012). The GC is a product of the closure of a Jurassic-Cretaceous aged back-arc basin, which opened north of the Pontide-Lesser Caucasus (LC) island arc during north-directed subduction of the Neothethys (e.g., Adamia, Alania, et al., 2011; Adamia et al., 1977; van der Boon et al., 2018; Cowgill et al., 2016; Gamkrelidze, 1986; van Hinsbergen et al., 2019; Vincent et al., 2016; Zonenshain & Le Pichon, 1986). The bedrock geology of the GC is broadly consistent with this history, being dominated by Cretaceous-Jurassic carbonates along the northern flank, flysch to molasse within much of the core of the range with isolated exposure of Variscan aged basement in the western GC, and LC Arc related volcanic and volcaniclastic rocks along the southern flank (Figure 1, e.g., Adamia, Zakariadze, et al., 2011; Cowgill et al., 2016; Forte et al., 2014; Saintot et al., 2006; Tye et al., 2020). The original geometry and dimensions of this GC back-arc basin, and thus the amount and style of convergence accommodated during the transition from subduction to collision, are debated (e.g., Cowgill et al., 2016, 2018; Vincent et al., 2016, 2018). However, recent plate reconstructions suggest a maximum NE-SW width of 200-300 km (van der Boon et al., 2018; van Hinsbergen et al., 2019), similar to the dimensions of remnants of this same back-arc basin in the South Caspian and Black Sea basins (Zonenshain & Le Pichon, 1986).

The closure of the GC back-arc basin represented the last in a series of similar intervening basin closures further south within the central Arabia-Eurasia collision (e.g., Cowgill et al., 2016; Golonka, 2004; van Hinsbergen et al., 2019; Vasey et al., 2020). The closure and shortening of the GC back-arc basin was accommodated at least in part by the northward subduction of oceanic to transitional crust, which originally floored the basin (e.g., Mumladze et al., 2015). A remnant of this subducted slab is preserved in the eastern GC (Mellors et al., 2012; Mumladze et al., 2015; Skolbeltsyn et al., 2014) and appears continuous with active, northward subduction of the South Caspian oceanic lithosphere beneath the middle Caspian Basin (Gunnels et al., 2020). No clear evidence of a slab is observed in the western GC, possibly due to slab detachment beneath this portion of the range (Figure 1, Mumladze et al., 2015) or, alternatively, a fundamentally different pre-existing basin architecture in the western GC (e.g., Adamia, Alania, et al., 2011) that did not result in formal subduction and where shortening was dominated by inversion of former high-angle rift structures (Vincent et al., 2016). However, the dominance of inversion tectonics in the western GC is largely inconsistent with more detailed structural observations that instead highlight the accretionary nature of this portion of the range (Trexler et al., 2022), consistent with a variety of broadscale observations of the geology of the range (e.g., Dotduyev, 1986; Philip et al., 1989). While definitive evidence of a past subduction zone in the western GC remains elusive, the surface response to a hypothesized slab detachment has been invoked to explain apparently excess amounts and rates of exhumation in the western GC (Forte et al., 2016; Vincent et al., 2020). The slab detachment mechanism is largely similar to earlier suggestions that dynamic support was important in the topographic compensation and uplift of the western GC (Ruppel & McNutt, 1990), though the original mechanism invoked was delamination of a thickened crustal root (e.g., Ershov et al., 1999, 2003; Mikhailov et al., 1999). However, the viability of the slab detachment mechanism in driving rapid exhumation within the core of the western GC remains unclear as it appears to require a spatially restricted isostatic response (Vincent et al., 2020) compared to much broader wavelength predictions from general models of slab detachment. Importantly, the dimensions of the response to slab detachment depends critically on detachment depth (e.g., Davies & von Blanckenburg, 1995; Duretz et al., 2011; Memiş et al., 2020), which is unknown for the hypothetical detachment event in the western GC. There is potential geophysical evidence of detached lithosphere beneath the western GC, with several tomographic models of the region illustrating an anomaly between 350-650 km depth that could be the remnants of a slab associated with former subduction in the western GC (e.g., Hafkenscheid et al., 2006; Koulakov et al., 2012; van der Meer et al., 2018; Zor, 2008). Similarly, there are suggestions that the western GC has begun to be southwardly underthrust by the Eurasian lithosphere in response to slab breakoff (Kaban et al., 2018). There remain diverse explanations for the possible origins of this seismic anomaly, with some (e.g., Koulakov et al., 2012) favoring older interpretations related to delamination of a crustal root (Ershov et al., 1999, e.g., 2003; Mikhailov et al., 1999). Generally, while permissive of a detached slab in the western GC, tomographic models of the region still contain meaningful disagreements in terms of the detailed lithosphere and mantle structure (see summaries in Ismail-Zadeh et al., 2020) and thus conclusively arguing for or against slab detachment in the western GC on the basis of tomography remains problematic. There is independent evidence for possible slab detachment from petrochronology, stable isotopic analyses of zircons, and thermomechanical modeling of the origin of magmas that erupted ignimbrite sequences around Mt. Elbrus in the western GC (Figure 1a), where Bindeman et al., (2021) relate their analysis of the silicic volcanism in the GC to this hypothesized slab detachment and date its occurrence to ~5 Ma.

At shallower crustal levels, the structural architecture of the GC has proven consistently controversial. Broadly, the GC is an anticlinorium, but displays an along-strike transition from a singly-vergent, south-directed orogenic wedge in the west to a doubly-vergent, but primarily south-directed orogenic wedge in the east (Forte et al., 2014) though the details of this are disputed (Alania, Tibaldi, et al., 2021). Since ~2 Ma, deformation has stepped out of the GC core to form a series of fold and thrust belts including the Rioni Fold and Thrust Belt (Trexler et al., 2020; Tsereteli et al., 2016), the Kura Fold and Thrust Belt (KFTB; Alania et al., 2015; Forte et al., 2010, 2013; Sukhishvili et al., 2020), and the Terek-Sunzha Fold and Thrust Belt (Figure 1; Forte et al., 2014; Sobornov, 1994, 1996). All of these structural systems appear significant in the accommodation of shortening within their respective extents, and the KFTB accommodates nearly all of the LC-GC convergence in the eastern half of the range since its establishment (Forte et al., 2010, 2013).

The location, geometry, and activity of structures within the interior of the GC are decidedly less clear. Numerous publications describe a master, orogen-spanning, south-directed structure usually referred to as the “Main Caucasus Thrust”, or MCT, as a primary shortening structure and possible cryptic suture (sensu Cowgill et al., 2016; Şengör, 1984), however the details of this structure are inconsistent across sources. The MCT is sometimes considered to be an active surface breaking thrust, and principally responsible for the accommodation of modern shortening (Allen et al., 2004; Jackson, 1992; Philip et al., 1989; Reilinger et al., 2006) or alternatively largely inactive for the last several million years, with slip from the foreland fold and thrust belts kinematically linked to the MCT at depth (Forte et al., 2010, 2013; Mosar et al., 2010), though this is the most relevant for the central and eastern GC, where the KFTB accommodates significant components of modern shortening. Thermochronology data across what may be the MCT in the western to central GC suggest that it was active in Cenozoic exhumation, but was likely not the only structure important for accommodating exhumation (Vasey et al., 2020). The geometry of this structure is variably described as either low (Dotduyev, 1986; Mosar et al., 2010) or high angle (Somin, 2011). Even the location of the MCT is uncertain with many considering it to be roughly coincident with the southern margin of the topography of the range (Forte et al., 2014, 2015; Kadirov et al., 2012; Saintot et al., 2006) while others place it in the interior of the orogen, near the topographic crest (Adamia, Zakariadze, et al., 2011; Mosar et al., 2010).

These discrepancies, coupled with new detailed field observations across many of the candidate MCT structures in the western and central GC led Trexler et al., (2022) to suggest that designating any structure as the "main" thrust was likely overly simplistic. They instead proposed a model of the southern GC as an imbricate fan of originally low-angle thrusts that sole to a common north-dipping detachment. The southern range front of the GC is then characterized by multiple south-directed structures accommodating relatively similar amounts of total shortening and exhumation, and propagating, primarily in-sequence, southward. Tye (2019) working in the extreme eastern GC propose a similar structural model for the range, i.e., an imbricate fan or accretionary prism style of deformation lacking a clear master structure, but do find that out-of-sequence propagation may be important, similar to prior results in this portion of the range within the KFTB and eastern GC (e.g., Forte et al., 2013, 2015). Critically, the detailed structural geometries within the core of the GC as revealed by recent work (Trexler et al., 2022; Tye, 2019) are largely inconsistent with a significant role for inversion of high-angle rift structures as sometimes considered for the western GC (e.g., Vincent et al., 2016) and are more consistent with models of accretionary orogens (e.g., Willett et al., 1993) where high angle structures in the interior of the range reflect rotation of formerly low-angle structures during accretion (e.g., Hoth et al., 2007).

2.2 Convergence and shortening in the Greater Caucasus

Published estimates of long-term rates of convergence between the Pontide-Lesser Caucasus block and the Eurasian margin and resulting total shortening within the GC vary widely (e.g., see discussion in Cowgill et al., 2016). Recent plate reconstructions suggest a maximum of 200-300 km of underthrusting or subduction has occurred since ~35 Ma, the timing of maximum extent of the GC back-arc basin (van der Boon et al., 2018). This estimate was confirmed and slightly refined in a larger, regional compilation of paleomagnetic data and plate reconstruction for the Mediterranean region by van Hinsbergen et al., (2019). Decadal scale GPS data show an order of magnitude along-strike eastward increase from <2 mm/yr to >14 mm/yr of NE-SW Lesser Caucasus motion with respect to stable Eurasia, driven by counter-clockwise rotation of the Lesser Caucasus block (Figure 1c, e.g., Kadirov et al., 2012; Reilinger et al., 2006; Sokhadze et al., 2018). In part, the slow rates of geodetic convergence paired with the high topography of the western GC led to the suggestion that additional sources of uplift, e.g., isostatic response to slab detachment, were necessary to explain the topography of the western portion of the range, but critically assumed this velocity gradient present in the GPS data to be a long-lived pattern (Forte et al., 2016).

The majority of modern LC motion appears to be accommodated via shortening along the southern flank of the GC, but with noticeable departures near the center of the range, where significant fractions of shortening are accommodated in the interior or along the northern edge (Figure 1; Forte et al., 2014). This shift in locus of shortening within the range may relate to the ongoing collision of the LC and GC structural systems in the center of the range (e.g., Alania, Beridze, et al., 2021; Banks et al., 1997; Forte et al., 2014; Nemčok et al., 2013; Sokhadze et al., 2018). It is unclear how far back in time these convergence gradients, either the broad counter-clockwise LC motion or the partitioning between shortening on the southern vs northern flank of the GC, can be extrapolated. Average rates of shortening in the KFTB since 1-2 Ma are consistent with the geodetic rate of GC-LC convergence at the same longitude, suggesting correspondence between geodetically measured LC-GC convergence and these average geologic rates since at least this time in the eastern GC (Forte et al., 2013). In contrast, over a similar time frame, geodetic shortening outpaces average geologic rates of shortening in the RFTB by nearly an order of magnitude, but this may simply reflect that significant portions of active shortening occur within the main range in this region and not on the foreland fold-thrust belt (Trexler et al., 2020).

2.3 Exhumation and Topography in the Greater Caucasus

The availability of low-temperature thermochronology data in the GC has increased in the last decade, though it is still spatially and system restricted (Figure 1; Avdeev, 2011; Avdeev & Niemi, 2011; Bochud, 2011; Král & Gurbanov, 1996; Tye, 2019; Vasey et al., 2020; Vincent et al., 2011, 2020). The majority of the available cooling ages are apatite fission track (~60%), with apatite (U-Th)/He being the next most represented (~20%) dates. Most of these data are also concentrated in the western GC, with >70% of samples located west of 44°E, and more importantly west of the hypothesized slab edge, with a much smaller concentration in the extreme eastern tip of the GC (Figure 1). There is also a distinct bias with respect to position within the range, with ~70% of the samples located north of the topographic crest, in the generally less structurally active portion of the range, sampled from the exposed pre-Mesozoic crystalline rocks in the western core (Figure 1; e.g., Forte et al., 2014; Saintot et al., 2006). More generally, the location of bedrock thermochronometer samples are primarily limited to portions of the range that expose either crystalline basement or volcanic or volcaniclastic rocks. With those caveats, and primarily with a focus on the western GC, a variety of workers have noted a consistent decrease of cooling ages toward the center of the range both in an along- and across-strike sense (Figure 1; Avdeev & Niemi, 2011; Forte et al., 2016; Král & Gurbanov, 1996; Vincent et al., 2020). In the core of the western GC, between Mt. Elbrus and Kazbegh (Figure 1a), both Avdeev & Niemi (2011) and Vincent et al., (2020) find a similar acceleration of cooling at ~5 Ma to 15-25°C/Myr, which depending on the assumed geothermal gradients and thermal modeling strategies, equates to Plio-Pleistocene exhumation rates of 0.75-1 mm/yr and total depths of exhumation of 5-12 km. Further west, the onset of this rapid cooling is slightly older, initiating at ~10-8 Ma (Vincent et al., 2020). Despite an earlier suggestion that this rapid cooling first documented by Avdeev & Niemi (2011) was a product of thermal perturbation by Cenozoic volcanism as opposed to an actual acceleration of rock uplift and exhumation (Vincent et al., 2018), subsequent analysis and additional sampling suggests limited influence of such thermal events (Vincent et al., 2020).

However, the tectonic interpretations of the onset of this rapid exhumation in the western GC vary. Avdeev & Niemi (2011) equate this increase in exhumation to initial collision of thickened, LC basement with the Eurasian margin, whereas Vincent et al., (2020) interpret the same signal as a pulse of exhumation driven by mantle upwelling, most likely linked to slab detachment (e.g., Mumladze et al., 2015) at ~10-5 Ma. Vincent et al., (2020) argue that the spatially restricted (~25-50 km wide in an across-strike direction) zone of rapid exhumation is a reflection of the isostatic response to slab detachment. They further argue that the relative narrowness of this rapidly uplifting zone, compared to the expectation of an across-strike wavelength of ~100-200 km observed in models of slab detachment (e.g., Duretz et al., 2011; Memiş et al., 2020), reflects the control of the isostatic response by basement structures (e.g., Cloetingh et al., 2013). Evaluating this hypothesis is hampered by the lack of thermochronology samples with well constrained cooling histories within the southwestern GC or further east, beyond the slab edge.

In the eastern sector of the GC, the more limited datasets from a series of theses broadly suggest a similar timing of initiation of rapid exhumation between ~10-5 Ma, but with more heterogeneity with some regions starting rapid exhumation closer to 20 Ma and others closer to 2-3 Ma (e.g., Avdeev, 2011; Bochud, 2011; Tye, 2019). Much of this variability appears to relate to the activation of specific structures, timing of accretion of particular terranes, and a complicated history of out-of-sequence deformation and post-cooling fold and fault related rotation within the eastern GC (Tye, 2019). Exhumation rates inferred from these samples are similarly variable, but mostly are 0.25-1 mm/yr (Avdeev, 2011; Bochud, 2011; Tye, 2019) overlapping with, or slightly lower than, rates estimated from the fastest cooling portions of the western GC.

At shorter timescales, estimates of decadal to millennial scale exhumation rates throughout the GC from modern sediment yields, heavy mineral assays, and ^{10}Be cosmogenic isotopes are broadly consistent and suggest a wide range of rates from 0.1 to >5 mm/yr, but with a spatially coherent pattern of low exhumation rates along the flanks and high exhumation rates exceeding 1 mm/yr within the core of the orogen (e.g., Forte et al., 2022; Vezzoli et al., 2014, 2020), broadly similar in spatial patterns to observations from low-temperature thermochronology. We focus on the recent millennial scale, ^{10}Be cosmogenic exhumation rate dataset (Forte et al., 2022) as this is the most geographically expansive of the available short term exhumation rates and spans the regions of the GC potentially driven by different rock uplift mechanisms (Figure 1d, S1). Forte et al., (2022) compared the GC topography in the form of normalized channel steepness (k_{sn}), a quantity shown to correlate to millennial scale erosion rate in a variety of orogenic settings (e.g., Adams et al., 2020; Cyr et al., 2010; DiBiase et al., 2010; Ouimet et al., 2009; Safran et al., 2005), to the GC millennial scale exhumation rates and found a singular and highly non-linear relationship between k_{sn} and exhumation rate, such that above an exhumation rate of ~0.3-0.5 mm/yr, the topography becomes relatively insensitive to increases in exhumation rate. In the GC, millennial scale exhumation rates are positively correlated with the GC-LC convergence rate and the proximity to the core of the range, suggesting that variability in rates primarily reflects tectonic forcing and resultant rates of rock uplift (Figure 1d, S1). Without knowledge of the highly non-linear relationship between topography and erosion rate, and also in part on the basis of a comparison between cooling ages and k_{sn}, or proxies thereof, Forte et al., (2016) argued that the similarity in topography of the GC along-strike likely implied similar rates of long-term rock uplift along-strike. If correct, this would imply a temporal change in exhumation rates between what is implied by cooling ages and cosmogenic ^{10}Be rates, something we consider in light of our new data presented here along with the improved understanding of the relationship between topography and millennial scale exhumation rate from Forte et al. (2022).

3 Material and methods

To understand the drivers of topographic growth of the GC through their transition from subduction to collision, it is necessary to integrate a variety of datasets. We first describe the methods for acquiring and analyzing a new detrital zircon (U-Th)/He dataset, which we use to partially fill the previously described gap in low-temperature thermochronology data along the strike of the GC. In order to place our detrital data into context with existing results, we then describe how we synthesize prior bedrock thermochronology data with our new detrital data. To evaluate whether the long-term view of exhumation derived from thermochronology is consistent with the more recent history of the range, we then develop a comparison between the thermochronologic exhumation rates and those from catchment averaged ^{10}Be cosmogenic isotopes which reflect average millennial rates. Finally, to place both the thermochronology and cosmogenic exhumation rates into a broader tectonic context and relate these back to the topographic growth of the GC, we derive an estimate of long-term convergence driving the formation of the GC. We then use this long-term convergence history to extrapolate simple predictions of the expected steady-state topography, allowing us to evaluate whether both the topographic form and exhumation rates over a range of timescales are consistent with a simple model of orogenic growth, or fundamentally require additional influences, like slab-detachment (Forte et al., 2016; Vincent et al., 2020).

3.1 Detrital zircon (U-Th)/He data and analysis

The primary new dataset we present consists of double-dated detrital zircons extracted from modern river sediments. These grains were dated using the Laser Ablation Double Dating (LADD) method at the ASU Group 18 laboratory (Horne et al., 2016; Tripathy-Lang et al., 2013). The LADD technique allows for measuring both (U-Th)/He and U-Pb ages in-situ on single zircons (Tripathy-Lang et al., 2013). This method is ideal for detrital thermochronology studies as it allows for the analysis of large sample sizes, can avoid averaging across growth zones of individual zircon grains, and avoids the need for alpha-ejection correction, which can be problematic when applied to detrital grains that have been abraded, broken, and/or have an unknown history of alpha-implantation (e.g., Evans et al., 2015; Glotzbach, 2019; Tripathy-Lang et al., 2013; Vermeesch et al., 2012). This is especially relevant for the samples described here as they are from modern detrital samples, which themselves are sourced primarily from sedimentary bedrock. Individual (U-Th)/He ages of grains dated by LADD generally are less precise than those dated by conventional means (Horne et al., 2016). However, the larger uncertainties on individual grain ages are generally outweighed by the benefit of being able to measure more statistically robust, i.e., larger, populations of grains (e.g., Brewer et al., 2003; Vermeesch, 2004). More generally, we applied a detrital zircon (U-Th)/He method because it; (1) provides a mechanism to fill in the thermochronologic data gap (e.g., Figure 1) which in part existed because of the difficulty of extracting enough suitable apatites or zircons from the flysch which dominates the exposed bedrock of the central and eastern GC and (2) allows for direct comparison of long-term and millennial erosion rates when paired with previously analyzed cosmogenic ^{10}Be erosion rates (e.g., Fox et al., 2015), like those recently presented by Forte et al., (2022). In the following sections we discuss the details of sample collection, laboratory analysis, and thermal modelling of the resulting data.

3.1.1 Sample collection

The seven detrital zircons samples we report here come from the same sample material as those used for millennial scale erosion rates from cosmogenic ^{10}Be concentration in quartz (Forte et al., 2022). Four of the samples (92215-1B, 92315-3B, CT15123, and 10215-4B) used were unprocessed secondary material from this original study, and three of the samples (82916-3A, 90416-1A, and 90516-1A) were sieved material with grain sizes less than 0.25 mm from the original samples used in Forte et al., (2022) where the larger fraction was processed for ^{10}Be concentration in quartz. All 7 samples have corresponding cosmogenic ^{10}Be erosion rates, the details of which are reported in Forte et al., (2022), but which we also provide in Table S1. In selecting these samples from the larger body available, we prioritized sites that would provide roughly continuous coverage along-strike of the GC, at least in part fill the data-gap in published low-temperature thermochronology data, but also overlap with existing bedrock data to check for correspondence (e.g., Figure 1), and contained lithologies likely to yield sufficient zircons for analysis. The sampled catchments vary in size from 6.7 to 231.8 km^2 in drainage area and generally span from 0.5 to >3 km in elevation (Figure S2, Table S1).

3.1.2 Sample preparation and detrital zircon LADD

After separation of zircons by standard methods including sieving, washing in water, separation by heavy liquids, and magnetic separation done by GeoSep Services, a target of 120 suitable zircon grains were picked from each of the seven detrital sediment samples based on grain size, primarily targeting grains with a major axis $\geq$70 μm, using a LEICA m125 picking scope and tweezers at Louisiana State University. This target number was not reached for all samples. Picked grains were shipped to the Group 18 Laboratory at Arizona State University. LADD analyses at ASU were conducted generally following the methods detailed in Horne et al. (2016). Typically for zircons, 25 μm diameter laser footprints are used for ^{4}He LA–GMS analyses and 65 μm footprints for U-Th-Pb LA–ICPMS analyses. However, in this case only four of the seven samples (90416-1A, 92315-3, 10215-4B and 82916-3A) had grains large and/or inclusion free enough to accommodate the 25-65 μm spot size tandem. For samples 90416-1A and 92315-3 all grains analyzed were able to fit the 25-65µm spot size tandem, but for sample 10215-4B and 82916-3A, 68 and 43 grains, respectively, were too small or are too affected by inclusions to be analyzed using the typical spot sizes. The small grains from those two samples and all grains of the remaining samples (CT15123, 92215-1B, 90516-1A) were analyzed using 15 µm and 50 µm diameter beam footprints for the helium and U-Th-Pb analyses respectively. We provide additional methodological details for the LADD technique as it pertains to our samples in the supplement (Section S1).

3.1.3 Thermal modelling

As discussed in the results, the majority of samples have a very wide distribution of (U-Th)/He grain ages, suggesting that a single-slope, linear age-elevation assumption is likely not valid. Interpretation of detrital data using simple age-elevation schemes (e.g., Brewer et al., 2003; Ruhl & Hodges, 2005) is generally impractical, and especially so in the absence of a priori knowledge of the expected age-elevation relationship, as is the case here. To deal with these complications, we use a recently developed approach for inverse thermal modeling of detrital thermochronology data (Gallagher & Parra, 2020) and implemented in QTQt v. 5.8.0. The underlying details of the multi-sample inverse scheme for both bedrock and detrital thermochronology data are described elsewhere (Gallagher, 2012; Gallagher et al., 2005; Gallagher & Parra, 2020). Here we briefly review relevant details, focusing on the detrital methodology for which the data are represented by an age distribution with all grains assumed to come from the same catchment.

When modeling detrital data, there are essentially two unknowns, the thermal history experienced by rocks exposed in the catchment and how those rocks are sampled by erosion at different elevations to produce a detrital sample. The sampling is referred to as the topographic sampling function, or TSF (e.g., Avdeev et al., 2011; Gallagher & Parra, 2020; Stock et al., 2006). The approach we use solves an inverse problem to estimate both of these unknowns. We produce a candidate thermal history by Markov chain Monte Carlo (McMC) sampling from a specified range for time and temperature values (the prior). The thermal history for the highest elevation in the catchment is represented by a series of time-temperature points. The number of points defining the thermal history is variable, and is drawn from a specified range (from 2 to 50 points). The thermal histories for other elevations are defined by an additional parameter, the temperature difference (or equivalent temperature gradient) between the highest and lowest elevations of the catchment, and linearly interpolating to the required elevation.

Having defined a thermal history over the elevation range of the catchment, we can predict an age-elevation profile. This is done by specifying a series of dummy samples, 10 at different elevations, covering the range of elevation in the catchment. Given the predicted age-elevation profile we sample this using the TSF (initially defined by the present day hypsometry) to generate a predicted detrital age distribution for the catchment. This predicted distribution can be quantitatively compared to the measured or observed distribution. The final step is to re-estimate the TSF using non-negative least squares to estimate weighting functions for sampling the predicted age-elevation profile (see Gallagher & Parra, 2020). If the estimated TSF improves the fit to the observed detrital distribution, then that is preferred to the default based on the present day hypsometry.

One implicit assumption of the modelling approach used by QTQt is that all portions of the sampled catchment experienced the same form of thermal history, so does not allow for discontinuities, i.e., active faults, within the catchment. Based on the locations of major structures from Trexler et al., (2022), three of our sample catchments, Katex – 82916-3A, Kish – 90416-1A, and Bum – 90516-1A, cross faults, but for both the Katex and Bum, the vast majority of the catchments are within one fault block and thus we do not consider this to be a major source of uncertainty. The Kish catchment is bisected by a fault (Figure S2), but is unclear the extent to which this influences our thermal modelling results for this sample. It is unknown when this fault was active or the amount of displacement it accommodated. It has generally been argued that faults within the southeastern portion of the GC, within which the Kish catchment is located, have not been active since at least ~2 Ma (e.g., Forte et al., 2010, 2014, 2015; Mosar et al., 2010), but we later assess whether activity on this fault may complicate the modelling of this sample.

Finally, one advantage of LADD derived data is that the predicted ages do not require alpha-ejection corrections (e.g., Tripathy-Lang et al., 2013). Therefore for modelling He diffusion with QTQt, we assume standard diffusion kinetic parameters for (U-Th)/He in zircon (Reiners et al., 2004), use an equivalent spherical radius for each grain based on the measured grain dimensions, but set the alpha ejection distance to zero. We provide additional detail on the specific parameters used within the QTQt runs in the supplement (Section S2).

3.1.4 Radiation damage considerations

One potentially important limitation of our modelling is that we do not include radiation damage effects, although its influence on He diffusivity can be significant in the interpretation of (U-Th)/He ages in zircon (e.g., Guenthner, 2021; Guenthner et al., 2013, 2014). In zircon, the effect of radiation damage is assessed in terms of the effective uranium (eU), and typically increasing eU leads a decreasing effective diffusivity up to a point when the radiation damage is so pervasive such that the effective diffusivity then decreases. For a given thermal history, this leads to a trend of increasing age with eU which can evolve to a decreasing age-eU trend if the radiation damage density is high enough. Thus, the potential for an influence of radiation damage on the measured (U-Th)/He age of a zircon is typically evaluated by assessing whether there is a clear relationship between the age and effective uranium (eU) concentration of individual grains within a sample. However, it is unclear the extent to which there would be an expectation of a meaningful age-eU relationship in a detrital thermochronology dataset, as a given detrital sample reflects random sampling of a potential different set of age-eU relationships reflecting different possible thermal histories from within a catchment. From a practical standpoint, it is also worth noting that no thermal modelling program that we are aware of (including QTQt) that is suitable for interpreting detrital data includes modeling of radiation damage in individual zircons within a detrital population. This suggests a critical need for the interpretation of large, detrital zircon (U-Th)/He datasets like the one we present here, but it is beyond the scope of this work to develop such a technique.

In the absence of a modelling framework that can fully account for potential eU variations in the inversion of a detrital zircon (U-Th)/He dataset, we take two independent approaches to evaluate the sensitivity of our results to potential age-eU effects. First, because ultimately in the modeling scheme we employ, the estimation of a thermal history from a detrital dataset is based on comparing the observed age distribution with candidate age distributions for a given thermal history, we evaluate whether there are significant differences in the age distributions of our samples on the basis of variations in eU. We test whether age distributions vary as a function of eU by binning ages by eU and statistically comparing the distributions to the whole population distribution, where statistically significant variation of eU based sub-populations would imply a potential biasing of the modelled thermal histories. Secondly, to assess whether our preferred thermal models from QTQt appear biased by neglecting eU variations, for each sample, we take the thermal history for the bottom and the top of the catchment and use the updated ZRDAAM model of Guenthner (2021) to predict what the age-eU relationships would be for these two thermal histories. The extent to which individual grains for a given catchment plot within the envelope defined by these two model age-eU relationships provides a crude metric for whether the observed age-eU patterns are compatible with having been drawn from a set of grains which experienced the range of thermal histories suggested by the QTQt model. Additional details of both of these approaches are described in the supplement (S3).

3.2 Synthesis of prior data

In addition to the new low-temperature detrital thermochronology data we present, we synthesize a variety of previously published results to develop a more synoptic view of the exhumation of the GC through time and how this relates to the topographic development of the range. This includes a synthesis of cooling models derived from bedrock thermochronology, a range wide estimation of millennial scale exhumation rates from detrital cosmogenic ^{10}Be, and finally integration with long-term estimates of convergence rate and growth of the GC topography.

3.2.1 Synthesis of bedrock cooling models

In order to put our new detrital thermochronology results into the a broader spatial and tectonic context, it is useful to compare them to published bedrock thermochronometer data. However, the possibility of making detailed direct comparisons on the basis of measured cooling ages of our new detrital thermochronology results with prior low-temperature thermochronology data in the GC is limited as ours is the only detrital thermochronology dataset in the region and there are only 14 published bedrock zircon (U-Th)/He dates within the GC (e.g., Figure 4d, S24; Avdeev & Niemi, 2011; Tye, 2019; Vasey et al., 2020). Similarly, none of the available bedrock thermochronology data lie within our sampled catchments, so we cannot formally model these together using QTQt. Instead, we focus on the implied cooling histories from thermal modelling as this provides a shared basis of comparison across different thermochronometric systems. For this, we elect to not remodel the earlier data as this represents a significant effort that is outside the scope of this particular paper and not all prior work provides sufficient information to accurately remodel their results. Instead, we compare our new cooling histories to those previously published. This approach has some disadvantages and caveats, specifically; (1) this removes significant numbers of prior analyses from consideration, including the large apatite fission track dataset of Král and Gurbanov (1996), and a variety of individual samples from other published works, i.e., any samples or suites of samples for which the original authors did not include a thermal model are excluded, (2) the modeled cooling histories incorporate different thermochronometric systems and as a result may be more or less sensitive to different portions of the cooling histories, and (3) the modeled cooling histories were derived from different thermal modeling approaches and programs, specifically prior results using QTQt (Gallagher, 2012), HeFTy (Ketcham, 2005), and CLOSURE and AGE2DOT (T. A. Ehlers et al., 2005), but all represent 1D thermal models. We provide a summary of these samples and the details of the published modelling incorporated into this analysis in Table S6.

To compare the cooling histories, we first digitize them using WebPlotDigitizer (Rohatgi, 2020), focusing on the mean or expected paths, as opposed to the full uncertainty envelopes or ranges of accepted models. We then calculate the average slopes of these time-temperature paths to estimate cooling rate as a function of time. As a simple basis for comparison, we then average the cooling rate over specific time intervals of 35-20, 20-10, 10-5, 5-0 Ma. For the detrital samples, there is not a single time-temperature path, so we first calculate a mean cooling rate for the given time intervals for both the top and bottom of the catchment and then calculate the mean cooling rate as the average of these two. In reailty, the relationship between cooling rate and exhumation rate is non-trivial because of the advection of heat and the evolving geothermal gradient in response to both rock uplift and erosion (e.g., Moore & England, 2001; Willett & Brandon, 2013), especially in thrust belts due to the potential importance of lateral motion (e.g., Batt & Brandon, 2002; Gilmore et al., 2018; Lock & Willett, 2008). In the absence of well constrained structural control for most of the sample locations, we make an extremely simple set of assumptions to translate these averaged cooling rates to exhumation rates by assuming a range of static geothermal gradients of 20-40°C/km and vertical exhumation paths (Figure 5a, 6b). In turn, we can take the thermal histories and the same assumed linear geothermal gradients and estimate the total amount of vertical exhumation that the modeled cooling histories would imply, in this case over the last 10 Ma (Figure 5b, 6a). Additional methodological details for how these estimates were derived is provided in the supplement (Section S4).

3.2.2 Estimation of millennial scale exhumation rate from ^{10}Be cosmogenic data and comparison with thermochronology

Even for cooling models which include apatite (U-Th)/He ages as a constraint, they generally will not be sensitive to the more recent, e.g., millennial scale, history of exhumation rate, and generally are only constrained up to the youngest cooling age included within a model. As we wish to evaluate whether there have been more recent changes in exhumation rate which may inform our understanding of the dominant mechanisms forming the topography of the GC, we incorporate estimates of exhumation rate derived from catchment averaged ^{10}Be cosmogenic isotopes. To assess the possibility of either acceleration or decelerations of rates between the long-term and millennial exhumation rates, it is necessary to compare the rates in the same locations. For our new detrital (U-Th)/He ages, we can directly compare the measured exhumation rate from cosmogenic ^{10}Be to the estimated exhumation rates from the detrital zircon (U-Th)/He. However, because none of the estimates of exhumation rates derived from our compilation of bedrock thermochronometers lie within any of the ^{10}Be catchments from Forte et al., (2022), we first must estimate the millennial scale exhumation rate in the bedrock sample locations. To do this, we use a simplified, power law form of the relationship between normalized channel steepness (k_{sn}) and millennial scale exhumation rates based on the stream power incision model (e.g., Kirby & Whipple, 2012; Whipple & Tucker, 1999), which was established in Forte et al., (2022) for the GC, and the k_{sn} at each bedrock sample location, averaged within a 5 km radius to estimate the millennial exhumation rate, similar to the methodology described by Adams et al., (2020) (Figure S26).

To compare the millennial and long-term rates of exhumation, it is useful to ratio the two rates, such that a value greater than 1 implies a recent increase in rate, whereas a ratio less than 1 implies a recent decrease in rate. Also in this context, and with our ultimate goal of assessing how the drivers of rock uplift are reflected in the topography of the GC, it is useful to consider what the fluvial response time of the topography would be to such a change in exhumation rate. In detail, the ratio between millennial and long-term exhumation rates is equivalent to the fractional change in uplift rate (f_U) that is used to calculate fluvial response time, or the time required for a long profile of a river to equilibrate to a step-change in rock uplift (Whipple, 2001). We review the relevant equations from Whipple (2001) in the supplement (Section S6), but in short, we use the same parameters from the stream power incision model that we use to estimate millennial scale exhumation rate along with the a relationship between drainage area and channel length (e.g., Hack, 1957) that we estimate from the basins sampled for cosmogenic ^{10}Be to calculate fluvial response time over a range of total stream lengths representative for the GC and a range of f_U.

3.2.3 Estimating long-term convergence rate and rock uplift rate

To relate estimates of exhumation rate along-strike to tectonics, and specifically to the driving mechanism for rock uplift, it would be ideal to compare exhumation or cooling rates with estimates of total shortening. However such upper plate shortening estimates are extremely limited (e.g., Cowgill et al., 2016). In their absence, we can compare cooling and exhumation rates to long-term records of plate convergence from recent regional plate reconstructions (van der Boon et al., 2018; van Hinsbergen et al., 2019). We derive a simple estimate of total convergence accommodated within the GC region over the same time frames as we average the cooling rates by using GPlates (Müller et al., 2018) to map the projected northeastern edge of the Pontide, Lesser Caucasus, and Talysh blocks, relative to the position of Eurasia (Seton et al., 2012) since 35 Ma, and differencing their positions along a N25°E azimuth. We provide additional details of this calculation in the supplement (Section S7).

3.2.4 Estimation of steady state fluvial relief

Finally, we wish to assess whether average rates of long-term convergence are compatible with observed rates of exhumation and the first-order topography of the GC and what this implies with regards to the dominant mechanisms for building the topography of the range. For this, we use the relatively simple parameterization of the growth and exhumation of a bivergent orogenic wedge developed by Whipple & Meade (2004). This parameterization treats orogenic topography as a balance between rock uplift driven by accretion into the range and exhumation by rivers, and allows us to predict the expected steady-state fluvial relief of the orogen. For this calculation, we need to estimate a variety of parameters including (1) basic aspects of the drainage network structure such as the relationship between the length of rivers and their drainage area, (2) details of the fluvial erosion mechanisms, (3) the width of the range and the distance between the edges of the range and the topographic crest, and (4) the rate of accretion into the orogen. For the aspects of the drainage network and details of the erosional mechanisms, we rely on the prior results and topographic analysis done by Forte et al., (2022), specifically using the same relationship between k_{sn} and ^{10}Be exhumation rates used to estimate the millennial scale exhumation rate throughout the GC. For basic geometric aspects of the range, we manually measure the width of the range, excluding the more recently formed fold-thrust belts, extract the position of the topographic crest, and then calculate a smoothed width for the two sides of the orogen, i.e., the pro-wedge, which faces the main direction of under-thrusting and the opposite retro-wedge. In the GC, we follow prior work and consider the southern side of the range the pro-wedge and the northern side of the range as the retro-wedge (Forte et al., 2014). Finally, to estimate accretion rate, we take the along-strike estimates of convergence rates described previously and assume either a 5 or 10 km thickness of material being accreted into the southern pro-wedge, which reflect the range of estimates of the depth to basement within the southern foreland of the GC (e.g., Alexidze et al., 1993), which Forte et al., (2016) used previously as a proxy for accretion thickness. We assume that uplift is distributed equally between the pro- and retrowedge and then combine all of the above to calculate an estimate of the steady-state fluvial relief of the GC to compare to the observed topography. We provide additional details in the supplemental methods (Section S8) and review relevant equations used from Whipple & Meade (2004).

4 Results

In the following sections, we provide an overview of both the analytical and thermal modelling results from each of our detrital thermochronologic samples. When discussing the thermal modelling results, we primarily focus on the late Cenozoic history (i.e., <35 Ma) as this is (1) the most relevant for understanding the recent exhumation history of the GC, (2) much of the history prior to this is not well constrained and the range of accepted models is relatively wide for this older history for most samples, and (3) this timing largely corresponds to the beginning of the closure of the Greater Caucasus back-arc basin (van Hinsbergen et al., 2019). When referencing cooling rates, we describe those estimated for the lowest elevation dummy sample, which typically represents a maximum cooling rate. The inferred timing of changes in cooling rates from the models will be the same for all catchment elevations because of the assumption of a single thermal history, but the magnitude of cooling rates can be lower for higher elevations within the catchment due to the imposition of the constraints on the present-day temperature lapse rate. We discuss the samples (and results) in order from west to east.

The LADD technique produces (U-Th)/He, ^{235}U-^{207}Pb, and ^{238}U-^{206}Pb ages for each zircon. We primarily focus on the (U-Th)/He ages as it is beyond the scope of this study to interpret the U-Pb ages, but display ^{238}U-^{206}Pb ages (e.g. Figure 2), and report all three ages, along with additional information for each analysis in Table S2. The discordance between ^{235}U-^{207}Pb and ^{238}U-^{206}Pb ages is a useful constraint for removing some grains from consideration in the thermal modelling (see Supplement). We report relevant topographic statistics for each sampled watershed in Table S1 and include topography of the sampled catchments and their hypsometry (Figure S2). The total number of reported grains (623 ages) is less than the total number of picked grains (794 grains), primarily because individual grains; (1) were too small to accommodate even the reduced footprint U-Th laser spot after polishing (93 grains), (2) did not survive the ablation process of both the U-Th-Pb and/or He laser spots (71 grains), or (3) yielded (U-Th)/He ages older than ^{206}Pb/^{238}U ages (7 grains). We summarize the outcomes of non-reported grains for each sample in Table S3. Additionally, parameters for and outcomes of the QTQt thermal modelling for each sample are reported in Table S4. We also provide summary lithologic maps (Figures S3, S6, S9, S12, S15, S18, S21) and report main depositional ages of units within each catchment in Table S5 based on a prior compilation (Forte, 2021). Also in the supplement, we provide detailed thermal modelling results including the full thermal history, the topographic sampling function (TSF), geothermal gradient history, implied age-elevation relationships, and comparisons between the observed and modeled age distributions (Figures S5, S8, S11, S14, S17, S20, S23). Finally, we consider the observed relationships between cooling age and eU (Figures S4, S7, S10, S13, S16, S19, and S22) and the extent to which radiation damage may influence our modeling results.

4.1 Kherla River – Sample 92215-1B

The sampled portion of the Kherla River catchment, a tributary to the Inguri in Georgia, drains predominantly interbedded sandstone and shale with minor phyllites and schists (Figure S3, Table S1). Bedrock within the catchment is dominated by Early Jurassic aged rocks with minor (<7%) exposures of Upper Paleozoic to Triassic (Table S5). The sample yielded 94 dateable zircons and all grains required the smaller 50 μm laser footprint for measuring U-Th concentrations. $^{206}Pb/^{238}U$ dates range from 2809 ± 15 Ma to 229.1 ± 2.0 Ma and (U-Th)/He dates range from 402.7 ± 13.2 Ma to 4.30 ± 0.16 Ma with >50% of these cooling ages being younger than 35 Ma (Figure 2a, Table S2).

Thermal modelling with QTQt suggests slow cooling until ~6 Ma, and then rapid cooling until the present (Figure 3A, S5). Cooling after 6 Ma starts at a rate of ~10°C/km, but gradually accelerated to a rate of ~60°C/km by the present (Figure 3a, 4c). The uncertainty on the initiation of cooling is skewed and implies that rapid cooling could have started as recently as 1 Ma at significantly faster rates. The preferred model suggests a geothermal gradient of ~28°C/km (Figure S5). The predicted expected age-elevation relationship is concave downward (Figure 4d) and the TSF from the preferred model implies contributions of grains effectively proportional to the catchment's hypsometry (Figure S5).

4.2 Khopuri River – Sample 92315-3B

The sampled portion of the Khopuri River catchment, a tributary to the Tskhenistkskali River in Georgia, exclusively drains interbedded Early Jurassic sandstones and shales (Figure S6, Table S1, S5). The sample yielded 85 dateable zircons, and 1 grain was excluded from thermal modeling. $^{206}Pb/^{238}U$ dates range from 2638 ± 34 Ma to 176.2 ± 2.8 Ma and (U-Th)/He range from 710 ± 25 Ma to 4.13 ± 0.18 with ~65% of these cooling ages being younger than 35 Ma (Figure 2b, Table S2).

Thermal modeling with QTQt suggests that much of the thermal history was dominated by isothermal holding or slight heating until ~11 Ma (Figure 4b, S8). Cooling which started at 11 Ma was originally slow at ~10°C/Myr until ~8 Ma, after which it increased to ~20°C/Myr, and finally increasing to ~40°C/Myr between ~1 Ma and the present (Figure 3b, 4c). Models generally suggested geothermal gradients of 40-50°C/km, with the preferred model implying a geothermal gradient of ~40°C/km. The predicted expected age-elevation relationship is concave downward (Figure 4d) and the preferred model TSF implies sampling of grains mostly proportional to the catchment hypsometry, but with some over representation of grains from the lowest elevations (Figure S8).

4.3 Tskhradzmula River – Sample CT15123

The sampled portion of the Tskhradzmula River catchment, a tributary to the Aragvi River in Georgia, mostly drains interbedded sandstones and shales with some limestone and minor clastics (Figure S9, Table S1). The majority of bedrock is Early to Middle Jurassic in age, with ~30% of the catchment being Late Jurassic to Valanginian (Table S5). The sample yielded 62 dateable zircons and 1 grain was excluded from thermal modeling. All grains required the smaller 50 µm laser footprint for measuring U-Th concentrations. $^{206}Pb/^{238}U$ dates range from 2598 ± 27 Ma to 0.115 ± 0.028 Ma and (U-Th)/He range from 193.1 ± 6.2 Ma to 0.023 ± 0.048 with ~93% of these cooling ages being younger than 35 Ma (Figure 2c, Table S2). The sample contains one grain which is likely derived from active Cenozoic volcanism in the GC with an extremely young $^{206}Pb/^{238}U$ and (U-Th)/He age, which we excluded from the QTQt modeling.

Thermal models generally suggest a period of heating between 50-10 Ma, and then cooling at ~25°C/Myr until the present (Figure 3c, 4c, S11). The preferred model implies geothermal gradients during much of the thermal history of ~38°C/km (Figure S11), but this did require restricting the allowable geothermal gradients beyond the defaults (Table S4). With a wider range of allowed geothermal gradients, several models with comparable acceptance rates suggested gradient of 50-60°C/km. In these higher gradient models, neither the timing of rapid cooling nor cooling rate during rapid cooling changed appreciably. In the preferred model, the predicted expected TSF implies elevated contributions of grains from the middle elevations of the catchment and virtually no grains from the upper portions of the watershed (Figure S11). Thus, the preferred model suggests a concave downward age-elevation relationship (Figure 4d), but that nearly all of the sampled grains come from the lower, quasi-linear portion of the age-elevation relationship (Figure S11).

4.4 Svianas Khevi River – Sample 10215-4B

The sampled portion of the Svianas Khevi River catchment, a tributary to the Stori River in Georgia, drains interbedded sandstones and shales and undifferentiated volcanic rocks (Figure S12, Table S1). Bedrock ages are predominantly Pliensbachian to Toarcian (Table S5). The sample yielded 88 dateable zircons, of these 68 grains required using a smaller 50 µm laser footprint for measuring U-Th concentrations. $^{206}Pb/^{238}U$ dates range from 2043 ± 29 Ma to 1.1 ± 1.2 Ma and (U-Th)/He range from 21.6 ± 1.8 Ma to 0.17 ± 0.18 Ma, excluding one older age of 120 ± 11 Ma. Approximately 98% of (U-Th)/He cooling ages are younger than 35 Ma (Figure 2d, Table S2). The sample contains three grains which are likely derived from active Cenozoic volcanism in the GC with extremely young $^{206}Pb/^{238}U$ and (U-Th)/He ages, which we exclude from the QTQt modeling.

Thermal modeling with QTQt suggests a heating event between 50-22 Ma (Figure S14). Slow cooling then began at a rate of ~3°C/Myr until 3 Ma after which it accelerated to 60-80°C/Myr (Figure 3d, 4c). The preferred model implies a geothermal gradient throughout much of the cooling history of ~32°C/km, but this did require restricting the allowable geothermal gradients beyond the defaults (Table S4). The predicted age-elevation relationship for the preferred model suggests a concave downward age-elevation relationship (Figure 4d) and the TSF suggests contributions of grains proportional to the hypsometry of the catchment (Figure S14). In detail the very small area occupied by the highest elevations of the catchment leads to the predominantly young ages (derived from lower elevations) observed in the detrital population (Figure 2d), implying that the majority of grains come from the portion of the catchment with a predicted quasi-linear age-elevation relationship.

4.5 Katex River – Sample 82916-3A

The sampled portion of the Katex River catchment in Azerbaijan drains primarily interbedded sandstones and shales with some contribution from sandstones with minor clastics (Figure S15, Table S1). The majority of bedrock in the catchment is Toarcian in age, with some (~30%) from Aalenian age rocks (Table S5). The sample yielded 102 dateable zircons, of these, 43 grains required using a smaller 50 µm laser footprint for measuring U-Th concentrations. One grain was excluded from thermal modeling. $^{206}Pb/^{238}U$ dates range from 2859 ± 26 Ma to 171.4 ± 2.1 Ma and (U-Th)/He range from 254.9 ± 8.3 Ma to 6.14 ± 0.59 Ma, with ~65% of (U-Th)/He cooling ages being younger than 35 Ma (Figure 2e, Table S2).

Thermal modelling with QTQt implies slow cooling until ~12 Ma, at which time cooling quickens to ~5°C/Myr, increasing to ~15-20°C/Myr after 6-7 Ma (Figure 3e, S17). The timing, and implied rate of cooling has relatively wide and skewed bounds of accepted models with initiation of slightly more rapid cooling potentially starting as late as ~6 Ma and proceeding much more rapidly at rates closer to 40°C/Myr. The preferred model implies that much of the thermal history occurred with a geothermal gradient of 35°C/km (Figure S17). The predicted expected age-elevation relationship is concave downward (Figure 4d) and the TSF suggests sampling of grains proportional to the catchment hypsometry (Figure S17).

4.6 Kish River – Sample 90416-1A

The sampled portion of the Kish River catchment in Azerbaijan is geologically relatively complex with no single lithology dominant (Figure S18, Table S1). Similarly, the ages of exposed bedrock in the catchment range from Late Jurassic to Cenomanian (Table S5). The Kish River catchment is the only catchment which includes significant portions of two sides of a fault (Figure S2). The sample yielded 81 dateable zircons and 3 grains were excluded from thermal modeling. $^{206}Pb/^{238}U$ dates range from 2885 ± 59 Ma to 97.8 ± 2 Ma and (U-Th)/He range from 498 ± 17 Ma to 4.15 ± 0.91 Ma, with ~57% of (U-Th)/He cooling ages being younger than 35 Ma (Figure 2f, Table S2).

The preferred thermal history from QTQt suggests isothermal holding to very slow cooling until ~7 Ma with rapid cooling at ~25°C/Myr after this time and increasing toward the present reaching a maximum around 40°C/Myr (Figure 3f, 4c). The range of time of rapid cooling in accepted models is relatively broad, varying from 7-3 Ma, with proportionally faster cooling rates (Figure 3f). The preferred model implies a geothermal gradient of ~33°C/km for much of the catchment's history (Figure S20), but this did require restricting the allowable geothermal gradients beyond the defaults (Table S4). The predicted expected age-elevation relationship is concave downward (Figure 4d) and the TSF suggests contributions of grains proportional to the hypsometry of the catchment (Figure S20).

4.7 Bum River – Sample 90516-1A

The sampled portion of the Bum River catchment in Azerbaijan is also geologically relatively complex with no single lithology dominant, but with undifferentiated volcanic rocks being the most common (Figure S21, Table S1). Ages of exposed bedrock vary from Aalenian to Hauterivian (Table S5). The sample yielded 111 dateable zircons, 1 grain was excluded from thermal modeling, and all grains required the smaller 50 µm laser footprint for measuring U-Th concentrations. $^{206}Pb/^{238}U$ dates range from 2449 ± 36 Ma to 160 ± 2.3 Ma and (U-Th)/He range from 397 ± 13 Ma to 1.3 ± 1 Ma, with ~96% of (U-Th)/He cooling ages being younger than 35 Ma (Figure 2g, Table S2).

Thermal modelling with QTQt implies isothermal holding to slight heating until 5 Ma (Figure 3g). After 5 Ma, rapid cooling at 20°C/Myr proceeded until ~4 Ma when cooling accelerated to 40°C/Myr until the present (Figure 3g, 4c). Using the default geothermal gradient ranges tended to suggest histories with low geothermal gradients of ~25°C/km. Restricting the range of allowable geothermal gradients produced models with comparable acceptance rates and higher geothermal gradients, with the preferred model suggesting a geothermal gradient closer to 30°C/km and more comparable to other samples (Figure S23). The predicted expected age-elevation relationship is concave downward and the TSF implied that grains from the lower elevations within the catchment are slightly overrepresented (Figures 4d, S23).

4.8 Evaluation of effects for age-eU relationships

To a first order, there are not clear, systematic relationships between eU and either (U-Th)/He or ^{238}U-^{206}Pb ages (Figures 2, S4, S7, S10, S13, S16, S19, and S22), but this is not necessarily unexpected from a detrital dataset. Of more relevance for a detrital dataset, where the distribution of ages is of critical importance with respect to interpreting the implied thermal history, comparing the (U-Th)/He age distribution within narrow eU bins to the whole population distribution within a sample does not reveal major, systematic differences (Figures S4, S7, S10, S13, S16, S19, and S22). This suggests that even if grains with a narrow range of eU were selected for modeling, that the derived thermal histories would not be significantly different. As an additional test, if we assume the preferred thermal histories as suggested by the QTQt modelling are correct and estimate what the predicted age-eU relationship would be for the thermal histories for the top and bottom of each catchment using the ZDRAAM model (Guenthner, 2021), the observed age-eU relationships for grains generally fall within the envelopes defined by these two thermal histories. While this does not imply that the modelled thermal histories would be the same if we were able to effectively model eU variations within the QTQt inversion, it does indicate that our preferred thermal histories are at least generally compatible with the observed age-eU relationships within our samples.

On average, both results suggest that our inferred thermal histories are not strongly biased by not formally including eU variations in the inversion and that there is likely not a strong, underlying age-eU relationship within the GC data. In terms of the inferred thermal histories, the absence of this effect potentially implies that any inferred major recent cooling episode can be treated as an upper limit in terms of the magnitude of cooling, and the inferred timing of cooling probably as a younger limit. Thus, while there could still be an influence of radiation damage, the relatively low dispersion in the ZHe ages (most of are younger than 100 Ma and many < 60 Ma) suggests that the lack of radiation damage modelling would not significantly modify our principal results and conclusions.

5 Discussion

5.1 Interpretation of cooling ages and thermal histories from detrital zircon (U-Th)/He

The large range of observed (U-Th)/He ages from all samples except the Tskhradzmula and Svianis Khevi catchments (e.g., Figure 2) and the highly curved, concave downward predicted age-elevation relationships suggested by the thermal modelling for all samples (Figure 4d, S24) are both consistent with most of these catchments exposing a portion of a fossil partial retention zone (PRZ, e.g., Stockli et al., 2000; Wolf et al., 1998). The inferred presence of a fossil PRZ from the thermal modeling in the Tskhradzmula and Svianis Khevi catchments at first seems surprising given the abundance of young (U-Th)/He ages in these samples. However, in detail, the QTQt models suggest that the majority of the older grains which would characterize the upper parts of a fossil PRZ were either not effectively sampled by erosional processes or were unlikely to be sampled because of the hypsometry of the catchment. The inferred base of a fossil PRZ effectively constrains the total amount of exhumation in all catchments to <5-10 km depending on the details of He diffusion and the isothermal holding time and/or thermal history prior to rapid exhumation (e.g., Reiners & Brandon, 2006). This range of total amounts of exhumation are consistent with prior estimates from elsewhere within the GC from in-situ bedrock samples (e.g., Avdeev & Niemi, 2011; Vincent et al., 2020). Similarly, while there are few complementary bedrock zircon (U-Th)/He ages to compare our results to (Avdeev & Niemi, 2011; Tye, 2019; Vasey et al., 2020), the age-elevation relationships implied by the QTQt modeling of the detrital samples are consistent with gross observed age-elevation patterns in bedrock sites after controlling for along- and across-strike position (Figure 4d, S24). In aggregate, the modeled thermal histories of our 7 samples are broadly similar, all being characterized by slow cooling, slight heating, or isothermal holding until the late Cenozoic, followed by rapid cooling until the present (e.g., Figures 3-4). In detail however, neither the timing of initiation of this rapid cooling, which varies from ~11-3 Ma but with the bulk of samples suggesting initiation of rapid cooling 8-5 Ma, or the rate of cooling after acceleration, which varies from 80-20°C/Myr, show any meaningful gross-scale along-strike patterns (Figure 4).

The presence of a fault within the Kish River catchment (90416-1A, Figure S2) does open the possibility that one of the underlying premises of the QTQt modeling scheme is violated for this sample, i.e., that there are no discontinuities within a modeled catchment. However, neither the age distribution (Figure 2f) or the modelled history (Figure 3f) for this catchment are particularly anomalous compared to the other catchments. Specifically, the presence of this fault, and a hypothetical major break in cooling ages across it, is generally not consistent with the observed cooling age population. Specifically, if a step change in cooling ages occurred across this fault, a more bimodal population would be expected between older ages sourced from the foot wall and younger ages sourced from the hanging wall, as opposed to the more continuous distribution observed (Figure 2f). Ultimately however, to fully assess whether the assumption of a continuous age-elevation relationship are valid for the Kish River catchment, or any of the other catchments, would require in-situ bedrock age-elevation transects.

5.2 Integration with prior thermochronologic results

At the most general level, comparison of cooling histories interpreted from previously published bedrock data and our new detrital data highlights that the detrital zircon (U-Th)/He results are similar to most prior bedrock results from comparable locations within the range (Figure 5-6, S25). This analysis also reveals similar spatial and temporal patterns described previously, specifically relatively slow or minimal cooling prior to ~10 Ma, an acceleration of cooling since ~10-5 Ma throughout the range, and more rapid cooling near the center of the range along-strike (e.g., Figures 5 and S25, Avdeev & Niemi, 2011; Král & Gurbanov, 1996; Vincent et al., 2020). Our new results do highlight for the first time that these patterns, previously described in the western GC, continue east along the range through the prior gap in thermochronologic data. Estimates of total amounts of vertical exhumation are broadly similar along-strike east of ~500 km (Figure 5b), after accounting for the position of the samples within the range (Figure 6). In an across strike sense, total amounts of exhumation are at a maximum along the southern range front of the GC, with lesser amounts near the topographic crest and the northern flank of the range, except in isolated areas (Figure 6a). Correspondingly, the rates of cooling are faster near the southern flank (Figure 6b, S25). It is worth noting that total amount of exhumation along-strike or across strike also shows no clear relation with where pre-Mesozoic basement rocks are exposed, suggesting that the geometry or thickness of the pre-collisional basin fill within the GC back-arc basin could have been significantly heterogeneous along-strike (Figures 1, 5, & 6; e.g., Vincent et al., 2016). For example, the areas along the southern range front, which appear to have experienced the most total exhumation since 10 Ma, are also areas without any basement exposure (Figure 6a). It is worth nothing however, that the supposition of originally thicker Mesozoic sediment cover within the eastern GC compared to the western GC is sensitive to the crustal-scale structural geometries in the respective portions of the range, which are not well constrained.

Consistently, interpreted total exhumation since 10 Ma is generally higher in the detrital samples than in the bedrock samples. There are two plausible, but not mutually exclusive, options to explain this pattern. The first is that majority of bedrock samples are primarily constrained by apatite fission track and (U-Th)/He (Table S6) and thus because of the lower closure temperature of the apatite systems compared to zircon (U-Th)/He, the total depth of exhumation from bedrock samples only constrained by apatite may be an underestimate. However, this is not the case for all bedrock samples, i.e., some do include higher temperature systems, and some samples have additional geologic constraints on the time-temperature history. The second option is that the difference depths in exhumation reflect a consequence of some aspect of the structural geometry of the range. The detrital samples come from the southern range front whereas the majority of bedrock samples for which there is thermal modelling come from the northern section of the range (e.g., Figure 6), so it is viable that these two areas reflect different structural domains. This hypothesis would be consistent with prior suggestions, that at least for the eastern GC, that the southern range front represents the long-term locus of exhumation, and that uplift of the region near the topographic crest is more recent (e.g., Forte et al., 2015). More broadly, in comparing across-strike differences in raw cooling ages, modeled cooling ages, or implied exhumation rates and total amounts of exhumation, it is important to consider that many of these samples lie within different fault blocks (e.g., Figures 4, 6-7). While the magnitudes of displacement across these structures are generally not well constrained (e.g., Trexler et al., 2022), it is ultimately not surprising that implied rates of exhumation or total amounts of exhumation differ between sites in the southern vs northern GC and across multiple different structures.

5.3 Comparing long-term and millennial scale exhumation rates

Comparison of the long-term exhumation rates from thermochronology with estimates of millennial scale exhumation rates from basin averaged cosmogenic ^{10}Be within the Greater and Lesser Caucasus (Forte et al., 2022) allows us to assess whether there have been more recent changes in exhumation. To a first order, after accounting for along- and across-strike position, the ^{10}Be derived rates in individual basins are broadly similar to estimated vertical exhumation rates for both bedrock and detrital thermochronometers within the same along- and across-strike position of the range (Figure 6b). However, the spatial separation of most of cosmogenic and thermochronologic samples make direct comparison more challenging, i.e., none of the bedrock thermochronology samples lie within a basin sampled for cosmogenic ^{10}Be. Using the millennial scale exhumation rates estimated from assuming a fixed, power law relation between k_{sn} and exhumation rate (e.g., Figure 7) allows for a more direct comparison, but with some important caveats. Specifically, Forte et al., (2022) demonstrate that assuming a single relationship between

k_{sn} and millennial scale exhumation rate is valid for the basins they measure, but the extent to which this relationship is applicable to the entire range is unclear. Similarly, the topography of areas currently glaciated, or which were glaciated during the LGM (Figure 7), may be sufficiently modified by glacial erosion so as to invalidate assumed relationship between k_{sn} and millennial scale exhumation rate (e.g., Anderson et al., 2006; Brocklehurst & Whipple, 2002). Finally, because of the non-linear nature of the relationship between k_{sn} and millennial scale exhumation (e.g., Figure S1), topography is inherently less sensitive to increases in exhumation rate above ~0.5 km/Myr (Forte et al., 2022), thus even large changes in exhumation rate above this threshold lead to small changes in topography and as a consequence the extrapolation of exhumation rate from topography is less certain in steep regions.

Caveats aside and taken at face value, comparing the estimation of millennial scale exhumation rates to long-term vertical exhumation rate, derived from the average cooling rate over the last 5 Ma, suggests that there are few areas where the two rates are similar within uncertainty, but that they still scale quasi-linearly with each other (Figure 8a). The ratio of measured or estimated ^{10}Be to thermochronologic exhumation rate reflects whether these rates appear to have accelerated or decelerated and is equivalent to the fractional change in uplift (f_U) that is often discussed in the context of the response of a fluvial network to a step-change in rock uplift (e.g., Whipple, 2001). Considering this ratio either as a function of along-strike distance or across-strike distance reveals some general patterns (Figure 8). Specifically, there is a consistent signal of acceleration in exhumation rates throughout much of the range, except in the area within ~200 east of the subducted slab edge, but this is anchored by only one of our new detrital samples (Figure 8). In the across-strike perspective, the apparent noise in the along-strike view appears instead to reflect a consistent trend of acceleration of exhumation rates north of the topographic crest, as opposed to south of the crest. This pattern is again consistent with suggestions made by Forte et al., (2015) on the basis of gross-scale geomorphology and landscape evolution modelling of a recent northward shift of deformation within the core of the range, at least for the central and eastern GC. Forte et al., (2015) interpreted this as a function of structure at depth, e.g., initiation of duplexing or a change in coupling between the subducted Kura Basin-Lesser Caucasus lithosphere and the overriding plate, but our data does not help to inform an exact cause for this pattern. The analysis here would suggest that a similar northward shift characterizes the western GC as well, though the extent to which the structural cause is the same as in the east remains unclear.

5.3 Implication for the tectonics of the Greater Caucasus

Cooling rates, or derived rates of vertical exhumation, do not show clear or systematic changes along-strike beyond the previously identified increase from the western tip toward the center of the range (e.g., Forte et al., 2016; Vincent et al., 2020), and most importantly, lack significant discontinuities across the hypothesized edge of the subducted slab (e.g., Figure 1 and 5). The samples from the Kherla (92215-1B) and Svianas Khevi catchments (10215-4B) are the only sites which show noticeably faster rates of cooling compared to nearby bedrock data, but the total amount of exhumation accommodated in both of these regions are comparable to other samples (Figure 5-6). Both the Kherla and Svianas Khevi catchments drains some of the steepest topography within the southern GC, and we consider this rapid and more recent exhumation reflected in the cooling history of these two sample could relate to local structural control, i.e., the Kherla and Svianas Khevi catchments are in different fault blocks from the nearby bedrock data (e.g., Figure 7b-c). Across our new detrital samples, estimates of total vertical exhumation over the last 10 Ma imply similar magnitudes along-strike east of ~500 km (Figure 5a). This along-strike similarity seems largely at odds with predictions of spatially restricted, elevated rates or magnitudes of exhumation within the western GC if primarily driven by slab detachment (e.g., Vincent et al., 2020).

Comparing along-strike patterns in estimated exhumation rate, total exhumation since 10 Ma, and the long-term convergence over the same time frame suggests that much of the observed increase in exhumation rates or total exhumation from the western tip toward the center of the range could be explained as a simple geometric consequence of increasing total convergence along-strike from the western tip to the center of the range (Figure 5). Barring major changes in orogenic architecture along-strike, a broad correspondence between long-term convergence rate and exhumation rates or depths would be expected. While there is variability within the estimates of total exhumation from bedrock samples, and the detrital samples show a more consistent pattern, the broadly similar rates of cooling and/or total exhumation east of ~500 km along-strike distance are also consistent with the similarity in implied convergence from plate models (Figure

5). It is, however, important to emphasize that the comparison of estimated amounts of convergence and total exhumation is relatively crude. The exact amounts of convergence would differ depending on the azimuth chosen and the resolution of the underlying plate model. For our estimate, the chosen azimuth is roughly perpendicular to the modern topographic strike of the range and the mean strike of bedding and foliation in the range (e.g., Trexler et al., 2022; Tye, 2019) and parallel to the modern convergence as indicated by GPS (e.g., Kadirov et al., 2012; Reilinger et al., 2006; Sokhadze et al., 2018). However, estimated directions of the velocity vectors of the reconstructed blocks vary along-strike and through time and often depart from a simple, consistent convergence direction, imparting some uncertainty into the analysis (Figure S27). Additionally, the translation from horizontal convergence and shortening to rock uplift or exhumation is highly dependent on the geometry and distribution of structures on which that shortening is accommodated, so more robust comparisons between the two would require constraints on crustal-scale structural geometries, which we generally do not have. Similarly, convergence, when accommodated by subduction or underthrusting, does not necessarily imply upper crustal shortening or resultant exhumation (e.g., Cowgill et al., 2016; van Hinsbergen et al., 2011; McQuarrie et al., 2003), so exact matches between convergence and exhumation would generally not be expected. Ultimately, the gross similarity in along-strike patterns in convergence compared to estimated total exhumation is permissive, but not diagnostic, of shortening driven by convergence as the primary mechanism for growing the topography of the GC, but we return to this idea in the final section.

Comparison of the total convergence (and thus derived estimates of rock uplift) from the plate reconstructions with backward extrapolation of the current along-strike trend in modern convergence, as measured by GPS within the Pontides, Lesser Caucasus, and southern foreland of the GC (e.g., Forte et al., 2014, 2022) highlights that the latter both (1) vastly overestimates the amount of total convergence along-strike and (2) is inconsistent with spatial patterns in either long-term convergence or cooling and exhumation rates from thermochronology. This is significant as Forte et al., (2016) used backward extrapolation of the modern convergence rate, and its failure when used in a simple model of orogenic growth to adequately explain the topography of the western GC, as part of the argument for the potential necessity of an isostatic response from slab detachment to explain the western GC topography.

Only in the comparison of millennial scale rates to average long-term (5-0 Ma) exhumation rates does there appear to be any spatially consistent patterns possibly related to the hypothesized slab edge, with an apparent acceleration in rate west of the slab edge (Figure 8). This observation leaves open the possibility that the acceleration west of the slab edge could reflect elevated rates of rock uplift and exhumation in the western GC driven by slab detachment (e.g., Mumladze et al., 2015; Vincent et al., 2020). Regardless of the underlying tectonic or geodynamic mechanism of this apparent acceleration, the cause of this acceleration needs to have occurred recently such that it is reflected in the topography and millennial rates, but not in exhumation rates averaged over the last 5 Ma. We attempt to estimate the timing of this acceleration by comparing the youngest thermochronometer age constraining a given thermal model with the fluvial response time for the implied change in uplift rate (Figure 8d). The youngest thermochronometer age represents a crude proxy for the robustness of a given long-term, 5-0 Ma average exhumation rate, i.e., a thermal model for which the youngest age constraining it is significantly older than 5 Ma suggests that the average rate between 5-0 Ma is likely not well constrained. Additionally, the youngest cooling age provides a sense of the true younger limit of the average rate, e.g., for a sample with the youngest cooling age of 2.5 Ma, the calculated 5-0 Ma average largely reflects an average rate between 5 and 2.5 Ma. We do emphasize that this is a crude estimate, especially for models constrained by apatite fission track where the track density may better constrain the younger portion of the thermal history than reflected by the age alone (e.g., Gallagher et al., 1998; Kohn et al., 2005). The fluvial response time of the landscape (e.g., Whipple, 2001) is relevant because the topography (and thus the estimate of millennial scale exhumation rate derived from the topography) is only representative of a new exhumation rate if sufficient time has passed for the landscape to have adjusted to a change in uplift rate. The lack of clear, consistent disequilibrium within the fluvial topography of the GC suggests that assuming topography is equilibrated to local rock uplift rates is valid, at least to a first order (Forte et al., 2016). Thus for a given sample, if not an artefact, the timing of an apparent increase in exhumation rate is constrained to having occurred between the youngest cooling age for a given sample and the fluvial response time for the implied fractional increase in exhumation rate. The comparison of these two timescales reveals that many of the samples indicating a change in exhumation rate could be thermal model artefacts, i.e., the youngest age is significantly older than the 5-0 Ma window so the extent to which the 5-0 Ma cooling history is constrained is unclear (Figure 8d). There are however samples across nearly the full along-strike length of the range, including all but one of our new detrital samples, that may reflect a real increase in exhumation rate. The youngest cooling ages for these samples are ~3-4 Ma, whereas depending on the length of the river network and the exact f_U, the fluvial response times are either comparable (for f_U near 1) or ~0.5-1 Ma (f_U near 10), providing a rough bracketing of when this apparent increase in exhumation rate could have occurred.

With a broad sense of when this acceleration may have occurred, we consider what this acceleration may represent tectonically. If the apparent acceleration in exhumation rates was driven by slab detachment (Forte et al., 2016; Mumladze et al., 2015; Vincent et al., 2020), it would require detachment to have occurred within this broad window of ~4 - 0.5 Ma. This range implies a slightly more recent time frame than that proposed by Vincent et al. (2020) or as suggested by modeling of silicic volcanism generation (Bindeman et al., 2021) both of which suggest detachment at ~5 Ma. However, models of the isostatic response to slab detachment do suggest a time lag between detachment and a change in rock uplift, which depending on the depth of the detachment could range from ~0.6 to 1.6 Myr (Duretz et al., 2011), so detachment could still occur at ~5 Ma and result in the acceleration of exhumation we see here. However, it is unclear whether a slab detachment mechanism would effectively explain either the along- or across-strike patterns in acceleration (Figure 8b-c). Vincent et al., (2020) argue that the narrow, 25-50 km wide across-strike zone of rapid uplift of the central-western GC (i.e., between Mt. Elbrus and the slab edge) hypothetically driven by slab detachment is restricted by basement faults and highlight that the expression of dynamic topography more broadly can be modulated by the presence of basement structures (e.g., Cloetingh et al., 2013). Fundamentally though, such basement structures are argued to change the internal form of the expected isostatic response, not the overall wavelength (Cloetingh et al., 2013). In contrast, numerical modeling of slab break off suggests ~100-200 km wide across-strike zones of isostatic uplift (e.g., Duretz et al., 2011; Memiş et al., 2020), comparable to the entire width of the GC. Thus, if this acceleration of rates in the western GC was related to slab detachment, it would be hard to reconcile with the f_U near or less than 1 in the three detrital samples west of the slab edge (Figure 8b). Similarly, while there could be more than one driver of changes in exhumation rates, slab detachment would not explain the consistent across-strike shift toward faster exhumation rates along the northern edge of the range observed in both the western and eastern GC (Figure 8c). Ultimately, integrating observations from along- and across-strike long-term exhumation patterns (Figure 5-6) and more recent millennial exhumation patterns (Figure 7-8) suggests that while there remain conflicting indications and the slab detachment model is still permissible with some of the data, we do not consider there to be robust evidence of the exhumation rates being strongly influenced by a slab detachment event beneath the western GC. Importantly, our data do not directly refute the occurrence of slab detachment or other form of mantle upwelling in the western GC, but rather highlight that there is not a clear indication of this event influencing either long-term or millenial exhumation rates. Given the variety of evidence consistent with detachment in the western GC (e.g., Bindeman et al., 2021; Hafkenscheid et al., 2006; Kaban et al., 2018; Koulakov et al., 2012; van der Meer et al., 2018; Mumladze et al., 2015; Zor, 2008) or more broadly the presence of some form of mantle upwelling beneath this portion of the range (e.g., Ershov et al., 2003; Faccenna & Becker, 2010; Motavalli-Anbaran et al., 2016; Ruppel & McNutt, 1990), the lack of a clear exhumation signal remains puzzling and highlights the necessity of more detailed work in the region to provide a more complete record of upper-crustal shortening along-strike, exhumation records in the central and eastern portion of the GC, and refined local tomographic models of the crustal and lithospheric structure as the majority of the geophysical results for the western GC rely on global datasets as opposed to local observations. Specifically, this hypothesis could be further constrained with more low-temperature thermochronology within the "thermochronologic gap" and perhaps the addition of more comparable detrital thermochronology datasets throughout the range to allow for more direct comparisons along- and across-strike. Additional bedrock or detrital thermochronology data north of the topographic crest within the thermochronologic gap would also help to constrain whether there is a consistent, along-strike increase in exhumation north of the topographic crest, which is hinted at in our data and would be consistent with prior suggestions, primarily made on the basis of topography (e.g., Forte et al., 2014, 2015).

If slab detachment is not necessary to explain either long-term exhumation rates or apparent changes in millennial exhumation rates, an alternative explanation for the cause of the recent northward shift of faster rates of exhumation implied by the comparison of the millennial and long-term rates could be the recent widening of the orogen and shifting of deformation into the forelands with the initiation of the KFTB, RFTB, and TSFTB, all of which appear to have formed around 1-2 Ma (e.g., Forte et al., 2010, 2013, 2014; Sukhishvili et al., 2020; Trexler et al., 2020) . More precise timing of the initiation of, and the detailed patterns of propagation and rates of shortening within these fold-thrust belts could further clarify this hypothesis. Alternatively, or perhaps in concert, this reorganization could reflect a response of the GC to collision with the northern margin of the LC thickened crust and structural systems (e.g., Alania, Beridze, et al., 2021; Banks et al., 1997; Forte et al., 2014; Nemčok et al., 2013).

Finally, it is worth reiterating that the extrapolation of millennial scale exhumation rates in many of the areas previously sampled for in-situ bedrock thermochronology should be approached with caution. Much of the signal indicative of recent acceleration of erosion/exhumation rate in the western GC comes from bedrock samples taken from areas glaciated during the LGM. In such regions; (1) fluvial landscape form could be obscured or modified by glacial activity (e.g., Anderson et al., 2006; Brocklehurst & Whipple, 2002) and thus the extrapolation of millennial erosion rates from k_{sn} could be problematic and (2) glacial erosion itself could contribute to increased rates of rock uplift (e.g., Hallet et al., 1996), though the extent to which glaciers can perturb long-term exhumation rates remains controversial (e.g., Adams & Ehlers, 2018; Michel et al., 2018). However, the observed patterns largely persist if formerly glaciated sample sites are removed from consideration, though the fidelity of the patterns are reduced (Figure 8). This again highlights the need for more thermochronology, and ideally ^{10}Be cosmogenic, exhumation rates outside of formerly glaciated areas.

5.4 Implications for the topographic growth of the Greater Caucasus

One of the original arguments in favor of the isostatic response to slab detachment contributing to the exhumation and topographic development of the western and central GC was inability of simple accretion models of orogens (Whipple & Meade, 2004) to explain the topography of the western and central portion of the range (Forte et al., 2016). However, a fundamental assumption in the analysis by Forte et al., (2016) was that the modern GPS convergence rates were applicable for at least for the last ~5 Ma, since the regional plate reorganization event that occurred throughout the Arabia-Eurasia collision zone and that may in part relate to the localization of deformation within the GC (e.g., Allen et al., 2004). In light of the observation that extrapolation of the GPS rate is inconsistent with plate models (e.g., Figure 5; van der Boon et al., 2018; van Hinsbergen et al., 2019), our synthesis of exhumation rates, our improved understanding of the details of the fluvial erosion of GC (Forte et al., 2022), and inconsistencies with the slab detachment mechanism of uplift for the western GC, we return to these simple models of orogenic growth to assess whether shortening and accretion is sufficient to explain the topography of the GC. Using the parameterization of Whipple & Meade (2004) and incorporating measurements of the width of the orogen (Figure 9a), accretion rates from assumed thicknesses of material entering the southern toe of orogen (i.e., the pro-wedge) and the along-strike patterns in averaged convergence rate since 10 Ma (Figure 5; van der Boon et al., 2018; van Hinsbergen et al., 2019), and the nature of the relationship between topography and erosion rates (Forte et al., 2022), allows us to estimate the average implied rate of rock uplift (Figure 9b), average amount of rock uplift (Figure 9c), and predicted steady-state fluvial relief for both the pro- and retro-wedge of the GC (Figure 9d). The broad similarity of the predicted steady-state fluvial relief for both the pro-wedge (south) and retro-wedge (north) and the mean elevation along the crest of the range suggests that, counter to what was originally proposed by Forte et al, (2016), that no additional significant sources of uplift, e.g., slab detachment, are required to explain the first order topography of the GC. The disagreement at the eastern tip of the range could reflect significantly thinner packages of material being accreted here than we assume, or that this portion of the range is still growing and thus the predicted steady-state relief reflect a projection, if average rates remain similar (Figure 9d). The average rates of rock uplift implied by this simple calculation (Figure 9b) are comparable to both the average rate of exhumation from low-temperature thermochronometers averaged over 5-0 Ma (Figure 5a, 6b), but also the average rate calculated over the 10-0 Ma time frame that we use to estimate the fluvial relief (Figure 9b). Total amounts of rock uplift that would result from these average 10-0 Ma rates of rock uplift operating since 10 Ma generally exceed total exhumation estimated from the thermochronometers over the 10-0 Ma period (Figure 9c), which is not all together unexpected because the total rock uplift would be the sum of exhumation and any surface uplift of the range that has occurred (e.g., England & Molnar, 1990).

The above estimation of expected relief and exhumation rates and magnitudes are admittedly a very simple model of orogenic growth and relief generation which does not account for the importance or evolution of individual structures and importantly assumes (1) an accretionary model is appropriate for the GC, (2) constant along-strike variation in width, (3) that all erosion is fluvial, and (4) that the fluvial erosional parameters all stay fixed (e.g., Whipple & Meade, 2004). The first assumption that the GC is well described as an accretionary orogen is broadly consistent with observations of the bedrock geology and gross structural architecture at a variety of scales (e.g., Dotduyev, 1986; Forte et al., 2014; Philip et al., 1989; Trexler et al., 2022; Tye, 2019). Such a model also broadly predicts thickened crust supporting the elevated topography of the range. Estimates of crustal thickness beneath the GC are variable (e.g., Figure 1f), but do suggest maximum crustal thicknesses 10-30 km greater than the average 30-35 km thickness of crust to the north of the range in the largely undeformed Russian platform (Motavalli-Anbaran et al., 2016; Robert et al., 2017; Shengelaya, 1984), consistent with significant crustal thickening. Some estimates do indicate that the amount of thickening in the western GC is less than observed in the eastern GC (Motavalli-Anbaran et al., 2016), but other estimates suggest broadly comparable amounts of thickening in the western and eastern GC (Figure 1f; Robert et al., 2017; Shengelaya, 1984). The second assumption of constant along-strike width is challenging to evaluate without a detailed chronology of initiation of individual structures, but there is no clear evidence of significant or consistent changes in the width of the range prior to the formation of the Plio-Pleistocene aged fold and thrust belts, and we exclude these regions from our width measurements. The third assumption that all erosion is fluvial, or fluvially mediated, is consistent with evidence from the topography that glacial erosion is minimal (e.g., Forte et al., 2014). The fourth assumption of constant erosional parameters is potentially problematic and harder to constrain. These parameters, that largely represent the relationship between erosion rates and topography, appear to be dictated by details of the hydrology of the range, which could have varied as a function of glacial-interglacial climate variability, more long-term regional climatic change, or the hypsometry history of the range itself (Forte et al., 2022), none of which are well constrained for the GC. Similarly, even assuming temporally constant hydroclimatic conditions, as described by Forte et al., (2022) the detailed patterns in the relationships between topography and millennial exhumation rate reflect a great diversity in modern hydroclimate, so the extent to which a singular relationship between topography and exhumation rate would remain if more samples were analyzed is unclear. Ultimately however, despite the simplicity and uncertainty of some of the assumptions required, the first-order correspondence between the estimated fluvial relief and exhumation patterns, the observed topography, and rates and magnitudes of exhumation independently derived from thermochronology highlight that this simple accretion model provides a reasonable explanation for the majority of the observations in the GC. Thus, on the basis of available data, we favor a traditional accretionary growth model for the GC as opposed to one that invokes a central role for dynamic topography or isostatic response to slab detachment to explain either the topographic or exhumation history of the range. This further highlights that evidence offered in previous work of a critical role for isostatic response to slab detachment in growing and maintaining the western GC topography (e.g., Forte et al., 2016; Vincent et al., 2020) suffered from lack of critical data further east and an incomplete assessment of both the long-term rates of convergence and the surface processes in the range.

6 Conclusions

Thermal modeling of new detrital (U-Th)/He ages, coupled with a synthesis of published bedrock cooling ages and thermal models, recently published plate reconstructions, structural observations, and ^{10}Be cosmogenic exhumation rates from the Greater Caucasus mountains does not support prior suggestions of a central role for the isostatic response to slab detachment as a primary mechanism for growing or maintaining the topography of the western Greater Caucasus. These results indicate that rapid exhumation of the Greater Caucasus began roughly between 10-5 Ma throughout much of the range, consistent with prior work, with the simplest explanation being that this reflects initial collision between Lesser Caucasus basement with Eurasia. Variability in the exact initiation time of rapid exhumation and exhumation rates between different parts of the range that lack clear along- or across-strike patterns likely reflect local structural details, but could also relate to along-strike gross-scale heterogeneity in the nature and thickness of the subducting and/or underthrusting Lesser Caucasus lithosphere or along-strike heterogeneity in pre-existing basin architecture and geometry.

Despite variability in timing and rates, our new zircon (U-Th)/He data suggests the preservation of a fossil partial retention zone in all of the sampled catchments, providing a similar limit for the total amount of exhumation and suggesting that along much of the length of the southern flank of the orogen, this has not exceeded ~5-10 km. Comparisons of long-term and millennial scale exhumation rates suggest a possible acceleration of rates in the western Greater Caucasus, but this pattern is not exclusive to the western portion of the range and appears to more consistently reflect an along-strike wide shift in the locus of faster exhumation to north of the topographic crest. The timing of this shift is broadly constrained to have occurred sometime between 4 – 0.5 Ma, potentially consistent with the timing of slab detachment, but also a variety of other potentially important tectonic events within the history of the Greater Caucasus. Importantly, the validity of the inference underlying this apparent acceleration in rates remains challenging to test because (1) extrapolations of millennial exhumation rates in the western Greater Caucasus are in part hampered by probable glacial modification of the landscape and (2) more broadly, the estimation of millennial exhumation rate throughout the Greater Caucasus relies on assuming that the relationship between topography and ^{10}Be cosmogenic exhumation rates, determined from a small group of spatially restricted samples, is broadly applicable to the entire range. To the extent that this apparent recent acceleration of exhumation rates are real, a more likely explanation is internal reorganization related to the widening of the orogen implied by the formation of numerous fringing fold-thrust belts and/or as a consequence of collision between the southern front of the GC and thickened crust of the Lesser Caucasus. Finally coupling improved estimates of both the amounts and average rates of plate convergence and our understanding of the details of erosion within the range compared to what was available for earlier interpretations, suggests that the average topography of the GC along-strike is suitably explained with traditional models of accretion, crustal shortening, and resulting rock uplift and does not fundamentally require additional sources of uplift, i.e., slab detachment.

In this work, we have treated exhumation of the Greater Caucasus simply, assuming linear and static geothermal gradients and vertical rock uplift. This simple framework is consistent with prior treatments of similar data in the range and we do not expect these assumptions to influence our core results, which focus on large-scale along-strike patterns. However, given the relative uncertainty of the gross structural architecture of the Greater Caucasus, we cannot exclude that the relative synchronicity of initiation of rapid exhumation within samples in the same general across-strike position within the range, which we interpret here primarily as being diagnostic of the initiation of orogenesis, could reflect large-scale changes in the trajectory of rocks, e.g., transition from a ramp to a flat within the basal decollement of the orogen. Future work should consider more explicitly the role of both lateral motion and time-varying thermal fields through the use of thermomechanical modelling to test the validity of our assumptions. These new data and syntheses help to constrain the first-order orogenic and topographic development of an archetypal example of a young orogen through its transition from subduction to continent-continent collision.

Data Availability Statement

All of the data is provided in the supplement as Excel files. The U-Pb and (U-Th)/He data along with sample locations and DEMs for each sample catchment are available here (https://doi.org/10.5281/zenodo.5609248).

Acknowledgements

Collection of samples used in this study was supported by National Science Foundation grant EAR-1450970 to A.M.F. and the analyses were supported by Louisiana Board of Regents Contract #LEQSF(2018-2019)-RD-A-02 awarded to A.M.F. We thank Charles Trexler, Alexander Tye, Nathan Niemi, Eric Cowgill, and Kelin Whipple for helpful conversations and sharing data that improved this manuscript. We thank Joel Leonard, Lasha Sukhishvili, Tea Godoladze, and Fakhraddin Kadirov for their help in collecting the original materials related to the ^{10}Be analyses. We also thank Michele Aigner and Achim Hermann for sharing time, equipment, and expertise that aided us in the processing of the detrital zircon (U-Th)/He samples. Finally, we thank Taylor Schildgen, Karl Lang, Kai Cao, and two anonymous reviewers for comments which improved earlier drafts of this paper.

Figure Captions

Figure 1 (a) Topography (SRTM 90) and bathymetry of the Greater Caucasus and surrounding regions. Circles are published apatite fission track dates, the most applied thermochronometer in the region, colored by cooling age (Avdeev, 2011; Avdeev & Niemi, 2011; Bochud, 2011; Král & Gurbanov, 1996; Tye, 2019; Vasey et al., 2020; Vincent et al., 2011, 2020). White boxes highlight the locations of the 7 detrital samples analyzed for zircon (U-Th)/He used in this study, labels are keyed to Figure 2. The dotted line outlines the extent of a 50 km wide swath taken along the topographic crest of the range, to which Figure 1c-f and several others are referenced. Also shown are the country borders of Georgia and Azerbaijan for reference. Abbreviations are RFTB – Rioni Fold-Thrust Belt, KFTB – Kura Fold-Thrust Belt, TSFB – Terek-Sunzha Fold-Thrust Belt, El – Mt. Elbrus, Ka – Mt. Kazbegh. (b) Simplified tectonic map, modified from Forte et al., (2014), with major faults from Trexler et al., (2022). (c) Grey swath shows maximum, minimum, and mean topography within the swath in 1a. Red swath is smoothed convergence between the Lesser Caucasus and southern margin of the Greater Caucasus as measured by GPS (Kadirov et al., 2012; Reilinger et al., 2006; Sokhadze et al., 2018). Details of the calculation of convergence are discussed in Forte et al, (2014) and Forte et al, (2022). Also shown are extents of where the Greater Caucasus is best described as a singly-vergent wedge (SVW) or a doubly-vergent wedge and where basement is exposed in the core of the range (e.g., Forte et al., 2014). (d) Circles, square, and triangles are cosmogenic ^{10}Be erosion rates (Forte et al., 2022), colored by distance from the topographic crest of the range (see color scale in 1f). Grey regions are estimated rates of the vertical uplift component of LC-GC convergence shown in 1c acting on either a 45° or 2° thrust fault for reference. See Figure S1 for locations of the ^{10}Be samples. (e) Cooling ages from apatite fission track data from 1a, colored by distance from center of the range. Apatite fission track data are displayed as this is the most commonly used technique in the range and thus reflects the maximum coverage of published thermochronology data in the range. (f) Earthquakes with magnitudes > 3 within 100 km of the topographic crest of the range, colored by distance from the crest and scaled by magnitudes (Di Giacomo et al., 2014; International Seismological Centre, 2020). Grey bar throughout figure shows approximate location of hypothesized subducted slab edge (e.g., Mumladze et al., 2015). Also shown are estimates of the maximum crustal thickness along the swath line from Shengelaya (1984), Motavalli-Anbarran et al., (2016), and Robert et al., (2017).

Figure 2 ^{206}Pb/^{238}U vs (U-Th)/He ages for all samples on a log-log scale. Density plots generated using DensityPlotter (Vermeesch, 2012) where filled plots are kernel density estimates with an adaptive bandwidth and the non-filled plots are probability density functions. Scatter plot of ages show 2σ uncertainty. Thick dashed line represents 1-1 line where ^{206}Pb/^{238}U and (U-Th)/He ages are equal. Individual grains are colored by their eU value. Open square ages indicate those excluded from the thermal modeling because of discordance. Individual plots of (U-Th)/He age vs eU are presented in the Supplement (Figures S4, S7, S10, S13, S16, S19, S22).

Figure 3 Preferred thermal models for each sampled catchment, showing expected time-temperature paths. Blue and red time-temperature paths are the expected paths for synthetic samples at the maximum and minimum elevations within the catchment, respectively and the shaded regions reflect 95% credible bounds for the accepted models. Gray lines are the expected time-temperature paths for 8 synthetic samples equally spaced in elevation within each catchment. We only show the last 35 Ma of the thermal models, refer to the relevant supplemental figures to see the complete thermal history for each sample.

Figure 4 (a) Major thrust faults from Trexler et al (2022) and average cooling rates between 5-0 Ma for selected bedrock thermochronometer sites (Circles; Avdeev, 2011; Avdeev & Niemi, 2011; Bochud, 2011; Vasey et al., 2020; Vincent et al., 2011, 2020) and the detrital sites from this study (squares). Faults are colored by the age of strata juxtaposed between hanging and footwall blocks. Rates for detrital samples reflect average cooling rates for the whole catchment, see the supplemental methods for more details, and positions of detrital samples reflect the centroid of watersheds. (b) Cooling rates and implied exhumation rates assuming linear 20 or 40°C/km geothermal gradients for the top of each sampled detrital catchment. Samples are ordered from west (Kherla) to east (Bum) and colored by the distance of their centroids along the swath (Figure 1a). (c) Same as 4b, but for the bottom of the catchment. (d) Predicted age elevation relationships for the detrital catchments (lines) compared to age elevation relationships for available bedrock zircon (U-Th)/He ages. Bedrock samples are colored by distance along the swath (see Figure 4c for color scale). More detailed consideration of the spatial relationships and age-elevation plots with a linear scale are presented in Figure S24.

Figure 5 (a) Averaged cooling rates as a function of distance along-strike. Individual symbols are average cooling rate from a thermally modelled history averaged between 5-0 Ma (upward pointing triangles), 10-5 Ma (squares), 20-10 Ma (diamonds), 35-20 Ma (downward point triangles). Lines are moving averages with a 50 km wide sliding window. Open symbols are from bedrock data (Avdeev, 2011; Avdeev & Niemi, 2011; Bochud, 2011; Vasey et al., 2020; Vincent et al., 2011, 2020) and filled symbols are the detrital data from this study. The right scales show equivalent vertical exhumation rates if either a 20°C/km or 40°C/km linear geothermal gradient is assumed. See text for additional description. Note there is a change in the vertical scale at 50°C/Myr. Positive cooling rates imply cooling, negative cooling rates imply heating. For the detrital datasets, cooling rate and derivatives are calculated as the average between the top and bottom modeled cooling paths. **(b)** Estimated total vertical exhumation since 10 Ma, see text and supplement for details. Individual symbols are colored by distance from topographic crest. Vertical whiskers represent different estimates depending on assumed geothermal gradient **(c)** Estimated amounts of convergence in the N25°E direction between the northern edge of the Pontides, Eastern Pontides, Lesser Caucasus, and Talysh and the center of the Greater Caucasus from the plate models of van der Boon et al, (2018) and van Hinsbergen et al, (2019), see Supplement for additional discussion. Amounts of convergence are averaged between 5-0, 10-5, 20-10, and 35-20 Ma, and total convergence between 35-0 Ma is shown in the solid black line. This is compared to the implied convergence over 35 Ma if the current N25°E motion of the Lesser Caucasus with respect to Eurasia from GPS represented long-term rates. Note different scale for the GPS convergence on the right.

Figure 6 (a) Sequence of swath profiles oriented N25°E and centered on the along-strike swath (Figure 1a) that approximates the topographic crest (TC). Each topographic swath is 20 km wide, but includes data projected from a 200 km wide swath centered on the topographic swath. Colored bars at the top show the projected positions of major structures (Figure 4a) within the topographic swath. Circles are projected position of bedrock thermochronometer sites where the height indicates the estimated vertical exhumation (left scale). Squares are projected centroid of detrital basins and the horizontal whiskers indicate the extent of each sampled basin and where the height indicates the estimated vertical exhumation (left scale). Vertical whiskers reflect the range of exhumation depending on assumed geothermal gradient. Both bedrock and detrital samples are colored by the distance along the strike from the across-strike swath centerline. (b) Underlying topography and fault positions the same as 6a. Height of projected data indicates estimated vertical exhumation rate averaged over 5-0 Ma (right scale). This includes the ^{10}Be basins from Forte et al. (2022), represented as triangles. Note that here the vertical exhumation rates for the thermochronology samples are calculated assuming a linear geothermal gradient of 30°C/km as this produced rates the most similar to those measured with ^{10}Be. Uncertainties on the thermochronology derived rates represent the standard deviation of the cooling rate during the 5-0 Ma period, assuming the same 30°C/km gradient.

Figure 7 (a) Map of millennial and longer term exhumation rates. The shading on the map is the estimated millennial rate using the relationship between topography and measured ^{10}Be exhumation rate using a power law form of the relationship, see main text and supplement for additional details. The individual symbols are the estimated average vertical exhumation rate since 5 Ma for bedrock (circles) and detrital (square) samples based on their modeled cooling histories and an assumed linear geothermal gradient of 30°C/km, see text for additional discussion. The white shaded region represents the portion of the topography influenced by LGM glaciation (Gobejishvili et al., 2011). (b) Expanded view of western GC with detrital basin outlines. (c) Expanded view of the central GC with detrital basin outlines. (d) Expanded view of the eastern GC with detrital basin outlines.

Figure 8 (a) Comparison between directly measured (black squares) or estimated (red circles) ^{10}Be exhumation rates and estimated vertical exhumation rate between 5-0 Ma from thermochronology. For the thermochronology vertical exhumation rates, the center symbol is assuming a linear 30°C/km gradient and horizontal whiskers assume a 20°C/km and 40°C/km gradient for the right and left whisker, respectively. Dashed line is a reference 1:1 relationship. ^{10}Be exhumation rates are estimated by using the normalized channel steepness and the power law fit between the two from Forte et al, (2022). Open symbols for bedrock samples are in areas glaciated during the LGM (Gobejishvili et al., 2011), where the estimation of exhumation rates from fluvial topography may be biased. See text and supplement for additional details (b) Ratio of either measured or estimated ^{10}Be rate and the estimated vertical exhumation rate between 5-0 Ma (f_U) assuming a linear 30°C/km as a function of distance along the swath in Figure 1a. Horizontal whiskers on detrital samples map extent of sampled basins. Vertical whiskers reflect the difference for assuming a 20°C/km and 40°C/km gradient for the upper and lower whiskers, respectively. (c) Same as 8b but in terms of distance from the topographic crest. (d) Comparison of the minimum cooling age that constrains a given thermal model with estimations of fluvial response time for a given f_U assuming an initial uplift rate of 0.5 km/Myr for river lengths of 50, 100, 250, and 500 km. Symbols are keyed to which mineral system provides the minimum constraint. Those with detrital zircon (U-Th)/He represent our detrital samples. Symbol colors indicate distance along-strike as indicated by the color bar in 8b.

Figure 9 (a) Measured widths of the Greater Caucasus along-strike for the full width and the pro- and retro-wedges. See supplement for additional discussion. (b) Estimated uplift rates along-strike using the convergence rate from the long-term convergence rate from plate models (van der Boon et al., 2018; van Hinsbergen et al., 2019) and assuming either a 5 or 10 km thickness of accreted material, which is within the range of estimated depths to basement along the southern foreland of the GC (Alexidze et al., 1993; Forte et al., 2016), and applied over the widths in 9a. Also plotted are exhumation rates from cooling rates averaged over 10-0 Ma and assuming a range of linear geothermal gradients 20-40°C/km, similar to how rates were calculated for Figures 5b and 6b. (c) Implied rock uplift applying the average uplift rate from 9b and assuming this rate was constant since 10 Ma, compared to estimated total exhumation from cooling histories over the same period. (d) Estimated steady-state fluvial relief using the simplified erosional parameters discussed in the text and the widths (9a) and uplift rates from accretion (9b).

References

Adamia, S., Lordkipanidze, M. B., & Zakariadze, G. S. (1977). Evolution of an active continental margin as exemplified by the alpine history of the Caucasus. *Tectonophysics*, *40*, 183–199.

Adamia, S., Zakariadze, G. S., Chkhotua, T., Sadradze, N., Tsereteli, N., Chabukiani, A., & Gventsade, A. (2011). Geology of the Caucasus: A Review. *Turkish Journal of Earth Sciences*, *20*, 489–544.

Adamia, S., Alania, V., Chabukiani, A., Kutelia, Z., & Sadradze, N. (2011). Greater Caucasus (Cavcasioni): A long-lived North-Tethyan Back-Arc Basin. *Turkish Journal of Earth Sciences*, *20*, 611–628.

Adams, B. A., & Ehlers, T. A. (2018). Tectonic controls of Holocene erosion in a glaciated orogen. *Earth Surface Dynamics*, *6*(1), 595–610. https://doi.org/10.5194/esurf-6-595-2018

Adams, B. A., Whipple, K. X., Forte, A. M., Heimsath, A. M., & Hodges, K. V. (2020). Climate controls on erosion in tectonically active landscapes. *Science Advances*, *6*(42). https://doi.org/10.1126/sciadv.aaz3166

Alania, V., Chabukiani, A. O., Chagelishvili, R. L., & Enukidze, O. V. (2015). Growth structures , piggy-back basins and growth strata of the Georgian part of the Kura foreland fold – thrust belt : implications for Late Alpine kinematic evolution. In M. Sosson, R. A. Stephenson, & S. A. Adamia (Eds.), *Tectonic Evolution of the Eastern Black Sea and*

Caucasus (Vol. 428). Geological Society of London Special Publication. https://doi.org/10.1144/SP428.5

Alania, V., Tibaldi, A., Bonali, F. L., Enukidze, O., & Russo, E. (2021). Structural Architecture of the Western Greater Caucasus Orogen: New Data from a Crustal-Scale Structural Cross-Section. In F. L. Bonali, F. Pasquaré Mariotto, & N. Tsereteli (Eds.), *Building Knowledge for Geohazard Assessment and Management in the Caucasus and other Orogenic Regions* (pp. 59–71). Dordrecht: Springer Netherlands. https://doi.org/10.1007/978-94-024-2046-3_5

Alania, V., Beridze, T., Enukidze, O., Chagelishvili, R., Lebanidze, Z., Maqadze, D., et al. (2021). The geometry of the two orogens convergence and collision zones in Central Georgia: New data from seismic reflection profiles. In F. L. Bonali, F. Pasquaré Mariotto, & N. Tsereteli (Eds.), *Building Knowledge for Geohazard Assessment and Management in the Caucasus and other Orogenic Regions* (pp. 73–88). Dordrecht: Springer Netherlands. https://doi.org/10.1007/978-94-024-2046-3

Alexidze, M. A., Gugunava, G. E., Kiria, D. K., & Chelidze, T. L. (1993). A three-dimensional stationary model of the thermal and thermoelastic fields of the Caucasus. *Tectonophysics*, *227*, 191–203.

Allen, M. B., Jackson, J., & Walker, R. (2004). Late Cenozoic reorganization of the Arabia-Eurasia collision and the comparison of short-term and long-term deformation rates. *Tectonics*, *23*, doi:10.1029/2003TC001530-doi:10.1029/2003TC001530.

Anderson, R. S., Molnar, P., & Kessler, M. A. (2006). Features of glacial valley profiles simply explained. *Journal of Geophysical Research*, *111*(F1), F01004. https://doi.org/10.1029/2005JF000344

Avdeev, B. (2011). *Tectonics of the Greater Caucasus and the Arabia-Eurasia orogen*. The University of Michigan.

Avdeev, B., & Niemi, N. A. (2011). Rapid Pliocene exhumation of the central Greater Caucasus constrained by low-temperature thermochronometry. *Tectonics*, *30*. https://doi.org/10.1029/2010TC002808

Avdeev, B., Niemi, N. A., & Clark, M. K. (2011). Doing more with less: Bayesian inversion of erosion models with detrital thermochonometric data. *Earth and Planetary Science Letters*, *305*, 385–395.

Axen, G. J., Lam, P. S., Grove, M., Stockli, D. F., & Hassanzadeh, J. (2001). Exhumation of the west-central Alborz Mountains, Iran, Caspian subsidence, and collision-related tectonics. *Geology*, *29*(6), 559–562.

Ballato, P., Uba, C. E., Landgraf, A., Strecker, M. R., Sudo, M., Stockli, D. F., et al. (2011). Arabia-Eurasia contitental collision: Insights from late Tertiary foreland-basin evolution in the Alborz Mountains, northern Iran. *Geological Society of America Bulletin*, *123*(1/2), 106–131. https://doi.org/10.1130/B30091.1

Banks, C. J., Robinson, A. G., & Williams, M. P. (1997). Structure and regional tectonics of the Achara-Trialet fold belt and the adjacent Rioni and Karli foreland basins, Republic of Georgia. In A. G. Robinson (Ed.), *Regional and petroleum geology of the Black Sea and surrounding region* (Vols. 1–68, pp. 331–346).

Barber, D. E., Stockli, D. F., Horton, B. K., & Koshnaw, R. I. (2018). Cenozoic Exhumation and Foreland Basin Evolution of the Zagros Orogen During the Arabia-Eurasia Collision, Western Iran. *Tectonics*, *37*(12), 4396–4420. https://doi.org/10.1029/2018TC005328

Batt, G., & Brandon, M. T. (2002). Lateral thinking: 2-D interpretation of thermochronology in convergent orogenic settings. *Tectonophysics*, *349*, 185–201.

Beaumont, C., Ellis, S., Hamilton, J., & Fullsack, P. (1996). Mechanical model for subduction-collision tectonics of Alpine-type compressional orogens. *Geology*, *24*(8), 675–678.

Bindeman, I. N., Colón, D. P., Wotzlaw, J.-F., Stern, R., Chiaradia, M., & Guillong, M. (2021). Young Silicic Magmatism of the Greater Caucasus, Russia, with implication for its delamination origin based on zircon petrochronology and thermomechanical modeling. *Journal of Volcanology and Geothermal Research*, *412*, 107173. https://doi.org/10.1016/j.jvolgeores.2021.107173

Bochud, M. (2011). *Tectonics of the Eastern Greater Caucasus in Azerbaijan*. University of Fribourg, Fribourg, Switzerland.

van der Boon, A., van Hinsbergen, D. J. J., Rezaeian, M., Gürer, D., Honarmand, M., Pastor-Galán, D., et al. (2018). Quantifying Arabia–Eurasia convergence accommodated in the Greater Caucasus by paleomagnetic reconstruction. *Earth and Planetary Science Letters*, *482*, 454–469. https://doi.org/10.1016/j.epsl.2017.11.025

Brewer, I. D., Burbank, D., & Hodges, K. V. (2003). Modelling detrital cooling-age populations: insights from two Himalayan catchments. *Basin Research*, *15*, 305–320.

Brocklehurst, S. H., & Whipple, K. X. (2002). Glacial erosion and relief production in the Eastern Sierra Nevada, California. *Geomorphology*, *42*, 1–24.

Cloetingh, S., Burov, E., & Francois, T. (2013). Thermo-mechanical controls on intra-plate deformation and the role of plume-folding interactions in continental topography. *Gondwana Research*, *24*(3–4), 815–837. https://doi.org/10.1016/j.gr.2012.11.012

Cowgill, E., Forte, A. M., Niemi, N. A., Avdeev, B., Tye, A. R., Trexler, C. C., et al. (2016). Relict basin closure and crustal shortening budgets during continental collision: An example from Caucasus sediment provenance. *Tectonics*, *35*, 2918–2947. https://doi.org/10.1002/2016TC004295

Cowgill, E., Niemi, N. A., Forte, A. M., & Trexler, C. C. (2018). Reply to Comment by Vincent et al. *Tectonics*, *37*(3), 1017–1028. https://doi.org/10.1002/2017TC004793

Cyr, A. J., Granger, D. E., Olivetti, V., & Molin, P. (2010). Quantifying rock uplift rates using channel steepness and cosmogenic nuclide-determined erosion rates: Examples from northern and southern Italy. *Lithosphere*, *2*(3), 188–198.

Davies, J. H., & von Blanckenburg, F. (1995). Slab breakoff: A model of lithosphere detachment and its test in the magmatism and deformation of collisional orogens. *Earth and Planetary Science Letters*, *129*, 85–102.

Di Giacomo, D., Storchak, D. A., Safronova, N., Ozgo, P., Harris, J., Verney, R., & Bondar, I. (2014). A New ISC Service: The Bibliography of Seismic Events. *Seismological Research Letters*, *85*(2), 354–360. https://doi.org/10.1785/0220130143

DiBiase, R. A., Whipple, K. X., Heimsath, A. M., & Ouimet, W. B. (2010). Landscape form and millennial erosion rates in the San Gabriel Mountains, CA. *Earth and Planetary Science Letters*, *289*(1–2), 134–144.

Dotduyev, S. I. (1986). Nappe Structure of the Greater Caucasus Range. *Geotectonics*, *20*(5), 420–430.

Duretz, T., Gerya, T., & May, D. A. (2011). Numerical modelling of spontaneous slab breakoff and subsequent topographic response. *Tectonophysics*, *502*, 244–256.

Eberhart-Phillips, D., Christensen, D. H., Brocher, T. M., Hansen, R., Ruppert, N. A., Haeussler, P. J., & Abers, G. A. (2006). Imaging the transition from Aleutian subduction to Yakutat collision in central Alaska, with local earthquakes and active source data: IMAGING ALEUTIAN TO YAKUTAT SUBDUCTION. *Journal of Geophysical Research: Solid Earth*, *111*(B11), n/a-n/a. https://doi.org/10.1029/2005JB004240

Ehlers, T. A., Chaudhri, T., Kumar, S., Fuller, C. W., Willett, S. D., Ketcham, R. A., et al. (2005). Computational Tools for Low-Temperature Thermochronometer Interpretation. *Reviews in Mineralogy and Geochemistry*, *58*(1), 589–622. https://doi.org/10.2138/rmg.2005.58.22

Ellis, S., & Beaumont, C. (1999). Models of convergent boudnary tectonics: implications for the interpetation of Lithoprobe data. *Canadian Journal of Earth Science*, *36*, 1711–1741.

Ellis, S., Beaumont, C., & Pfiffner, A. (1999). Geodynamic models of crustal-scale episodic tectonic accretion and underplating in subduction zones. *Journal of Geophysical Research*, *104*(B7), 15,115-169,190.

England, P. C., & Molnar, P. (1990). Surface uplift, uplift of rocks, and exhumation of rocks. *Geology*, *18*, 1173–1177.

Ershov, A. V., Brunet, M.-F., Korotaev, M. V., Nikishin, A. M., & Bolotov, S. N. (1999). Late Cenozoic burial history and dynamics of the Northern Caucasus molasse basin: implications for foreland basin modelling. *Tectonophysics*, *313*, 219–241.

Ershov, A. V., Brunet, M.-F., Nikishin, A. M., Bolotov, S. N., Nazarevich, B. P., & Korotaev, M. V. (2003). Northern Caucasus basin: thermal history and synthesis of subsidence models. *Sedimentary Geology*, *156*, 95–118.

Evans, N. J., McInnes, B. I. A., McDonald, B., Danišík, M., Becker, T., Vermeesch, P., et al. (2015). An in situ technique for (U–Th–Sm)/He and U–Pb double dating. *Journal of Analytical Atomic Spectrometry*, *30*(7), 1636–1645. https://doi.org/10.1039/C5JA00085H

Faccenna, C., & Becker, T. W. (2010). Shaping mobile belts by small-scale convection. *Nature*, *465*, 602–605. https://doi.org/10.1038/nature09064

Forte, A. M. (2021). *Lithologic compilation of basins sampled for cosmogenic 10BE in the Greater Caucasus Mountains*. Retrieved from https://doi.org/10.5281/zenodo.5752511

Forte, A. M., Cowgill, E., Bernardin, T., Kreylos, O., & Hamann, B. (2010). Late Cenozoic deformation of the Kura fold-thrust belt, southern Greater Caucasus. *Geological Society of America Bulletin*, *122*(3/4), 465–486.

Forte, A. M., Cowgill, E., Murtuzayev, I., Kangarli, T., & Stoica, M. (2013). Structural geometries and magnitude of shortening in the eastern Kura fold-thrust belt, Azerbaijan: Implications for the development of the Greater Caucasus Mountains. *Tectonics*, *32*. https://doi.org/10.1002/tect.20032

Forte, A. M., Cowgill, E., & Whipple, K. X. (2014). Transition from a singly vergent to doubly vergent wedge in a young orogen: The Greater Caucasus. *Tectonics*, *33*(11), 2077–2101. https://doi.org/10.1002/2014TC003651

Forte, A. M., Whipple, K. X., & Cowgill, E. (2015). Drainage network reveals patterns and history of active deformation in the eastern Greater Caucasus. *Geosphere*, *11*(5). https://doi.org/10.1130/GES01121.1

Forte, A. M., Whipple, K. X., Bookhagen, B., & Rossi, M. W. (2016). Decoupling of modern shortening rates, climate, and topography in the Caucasus. *Earth and Planetary Science Letters*, *449*, 282–294. https://doi.org/10.1016/j.epsl.2016.06.013

Forte, A. M., Leonard, J. S., Rossi, M. W., Whipple, K. X., Heimsath, A. M., Sukhishvili, L., et al. (2022). Low variability runoff inhibits coupling of climate, tectonics, and topography in the Greater Caucasus. *Earth and Planetary Science Letters*, *584*. https://doi.org/10.1016/j.epsl.2022.117525

Fox, M., Leith, K., Bodin, T., Balco, G., & Shuster, D. L. (2015). Rate of fluvial incision in the Central Alps constrained through joint inversion of detrital 10Be and thermochronometric data. *Earth and Planetary Science Letters*, *411*, 27–36. https://doi.org/10.1016/j.epsl.2014.11.038

Gallagher, K. (2012). Transdimensional inverse thermal history modeling for quantitative thermochronology. *Journal of Geophysical Research: Solid Earth*, *117*(B2), n/a-n/a. https://doi.org/10.1029/2011JB008825

Gallagher, K., & Parra, M. (2020). A new approach to thermal history modelling with detrital low temperature thermochronological data. *Earth and Planetary Science Letters*, *529*, 115872–115872. https://doi.org/10.1016/j.epsl.2019.115872

Gallagher, K., Brown, R., & Johnson, C. (1998). FISSION TRACK ANALYSIS AND ITS APPLICATIONS TO GEOLOGICAL PROBLEMS. *Annual Review of Earth and Planetary Sciences*, *26*(1), 519–572. https://doi.org/10.1146/annurev.earth.26.1.519

Gallagher, K., Stephenson, J., Brown, R., Holmes, C., & Fitzgerald, P. G. (2005). Low temperature thermochronology and modeling strategies for multiple samples 1: Vertical profiles. *Earth and Planetary Science Letters*, *237*(1–2), 193–208.

Gamkrelidze, I. P. (1986). Geodynamic evolution of the Caucasus and adjacent areas in alpine time. *Tectonophysics*, *127*, 261–277.

Gavillot, Y., Axen, G. J., Stockli, D. F., Horton, B. K., & Fakhari, M. D. (2010). Timing of thrust activity in the High Zagros fold-thrust belt, Iran, from (U-Th)/He thermochronometry: TIMING OF THRUST ACTIVITY IN HIGH ZAGROS. *Tectonics*, *29*(4), n/a-n/a. https://doi.org/10.1029/2009TC002484

Gilmore, M. E., McQuarrie, N., Eizenhöfer, P. R., & Ehlers, T. A. (2018). Testing the effects of topography, geometry, and kinematics on modeled thermochronometer cooling ages in the eastern Bhutan Himalaya. *Solid Earth*, *9*(3), 599–627. https://doi.org/10.5194/se-9-599-2018

Glotzbach, C. (2019). Increasing the accuracy of (U-Th(-Sm))/He dating with 3D grain modelling. *Chemical Geology*, 13.

Gobejishvili, R., Lomidze, N., Tielidze, L., & van der Meer, J. J. M. (2011). Late Pleistocene (Würmian) Glaciations of the Caucasus. In J. Ehlers, P. L. Gibbard, & P. D. Hughes (Eds.), *Quaternary glaciations - Extent and chronology* (Vols. 1–15, pp. 141–147). Amsterdam: Elsevier.

Golonka, J. (2004). Plate tectonic evolution of the southern margin of Eurasia in the Mesozoic and Cenozoic. *Tectonophysics*, *381*, 235–273.

Guenthner, W. R. (2021). Implementation of an Alpha Damage Annealing Model for Zircon (U-Th)/He Thermochronology With Comparison to a Zircon Fission Track Annealing Model. *Geochemistry, Geophysics, Geosystems*, *22*(2). https://doi.org/10.1029/2019GC008757

Guenthner, W. R., Reiners, P. W., Ketcham, R. A., Nasdala, L., & Giester, G. (2013). Helium diffusion in natural zircon: radiation damage, anisotropy, and the interpretation of zircon

(U-TH)/He thermochronology. *American Journal of Science*, *313*(3), 145–198. https://doi.org/10.2475/03.2013.01

Guenthner, W. R., Reiners, P. W., & Tian, Y. (2014). Interpreting date-eU correlations in zircon (U-Th)/He datasets: A case study from the Longmen Shan, China. *Earth and Planetary Science Letters*, *403*, 328–339. https://doi.org/10.1016/j.epsl.2014.06.050

Gunnels, M., Yetrimishli, G., Kazimova, S., & Sandvol, E. (2020). Seismotectonic evidence for subduction beneath the Eastern Greater Caucasus. *Geophysical Journal International*, *224*(3), 1825–1834. https://doi.org/10.1093/gji/ggaa522

Hack, J. T. (1957). *Studies of longitudinal stream profiles in Virignia and Maryland* (pp. 97–97).

Hafkenscheid, E., Wortel, M. J. R., & Spakman, W. (2006). Subduction history of the Tethyan region derived from seismic tomography and tectonic reconstructions. *Journal of Geophysical Research*, *111*(B8), B08401. https://doi.org/10.1029/2005JB003791

Hallet, B., Hunter, L., & Bogen, J. (1996). Rates of erosion and sediment evacuation by glaciers: A review of field data and their implications. *Global and Planetary Change*, *12*(1–4), 213–235. https://doi.org/10.1016/0921-8181(95)00021-6

Harris, R., Vorkink, M. W., Prasetyadi, C., Zobell, E., Roosmawati, N., & Apthorpe, M. (2009). Transition from subduction to arc-continent collision: Geologic and neotectonic evolution of Savu Island, Indonesia, 20.

van Hinsbergen, D. J. J., Kapp, P. A., Dupont-Nivet, G., Lippert, P. C., DeCelles, P. G., & Torsvik, T. H. (2011). Restoration of Cenozoic deformation in Asia and the size of Greater India. *Tectonics*, *30*(TC5003). https://doi.org/10.1029/2011TC002908

van Hinsbergen, D. J. J., Torsvik, T. H., Schmid, S. M., Matenco, LC., Maffione, M., Vissers, R. L. M., et al. (2019). Orogenic architecture of the Mediterranean region and kinematic reconstruction of its tectonic evolution since the Triassic. *Gondwana Research*. https://doi.org/10.1016/j.gr.2019.07.009

Horne, A. M., van Soest, M. C., Hodges, K. V., Tripathy-Lang, A., & Hourigan, J. K. (2016). Integrated single crystal laser ablation U/Pb and (U-Th)/He dating of detrital accessory minerals - Proof-of-concept studies of titanites and zircons from the Fish Canyon tuff. *Geochimica et Cosmochimica Acta*, *178*, 106–123. https://doi.org/10.1016/j.gca.2015.11.044

Hoth, S., Hoffmann-Rothe, A., & Kukowski, N. (2007). Frontal accretion: An internal clock for bivergent wedge deformation and surface uplift. *Journal of Geophysical Research*, *112*, B06408–B06408. https://doi.org/10.1029/2006JB004357

International Seismological Centre. (2020). *On-line Event Bibliography*. Retrieved from https://doi.org/10.31905/EJ3B5LV6

Ismail-Zadeh, A., Adamia, S., Chabukiani, A., Chelidze, T., Cloetingh, S., Floyd, M., et al. (2020). Geodynamics, seismicity, and seismic hazards of the Caucasus. *Earth-Science Reviews*, *207*, 103222. https://doi.org/10.1016/j.earscirev.2020.103222

Jackson, J. (1992). Partitioning of strike-slip convergent motion between Eurasia and Arabia in eastern Turkey and the Caucasus. *Journal of Geophysical Research*, *97*, 12,412-471,479.

Jamieson, R. A., & Beaumont, C. (2013). On the origin of orogens. *Geological Society of America Bulletin*, *125*(11–12), 1671–1702. https://doi.org/10.1130/B30855.1

Kaban, M. K., Petrunin, A. G., El Khrepy, S., & Al-Arifi, N. (2018). Diverse Continental Subduction Scenarios Along the Arabia-Eurasia Collision Zone. *Geophysical Research Letters*, *45*(14), 6898–6906. https://doi.org/10.1029/2018GL078074

Kadirov, F., Floyd, M., Alizadeh, A., Guliev, I., Reilinger, R., Kuleli, S., et al. (2012). Kinematics of the eastern Caucasus near Baku, Azerbaijan. *Natural Hazards*, *63*, 997–1006.

Kao, H., Huang, G.-C., & Liu, C.-S. (2000). Transition from oblique subduction to collision in the northern Luzon arc-Taiwan region: Constraints from bathymetry and seismic observations. *Journal of Geophysical Research: Solid Earth*, *105*(B2), 3059–3079. https://doi.org/10.1029/1999JB900357

Ketcham, R. A. (2005). Forward and Inverse Modeling of Low-Temperature Thermochronometry Data. *Reviews in Mineralogy and Geochemistry*, *58*(1), 275–314. https://doi.org/10.2138/rmg.2005.58.11

Kirby, E., & Whipple, K. X. (2012). Expression of active tectonics in erosional landscapes. *Journal of Structural Geology*, *44*, 54–75.

Kohn, B. P., Gleadow, A. J. W., Brown, R. W., Gallagher, K., Lorencak, M., & Noble, W. P. (2005). Visualizing Thermotectonic and Denudation Histories Using Apatite Fission Track Thermochronology. *Reviews in Mineralogy and Geochemistry*, *58*, 527–565. https://doi.org/10.2138/rmg.2005.58.20

Koulakov, I., Zabelina, I., Amanatashvili, I., & Meskhia, V. (2012). Nature of orogenesis and volcanism in the Caucasus region based on results of regional tomography. *Solid Earth Discussions*, *4*, 641–662.

Král, J., & Gurbanov, A. G. (1996). Apatite Fission Track Data from the Greater Caucasus pre-Alpine Basement. *Chemie Der Erde*, *56*, 177–192.

Lester, R., McIntosh, K., Van Avendonk, H. J. A., Lavier, L., Liu, C.-S., & Wang, T. K. (2013). Crustal accretion in the Manila trench accretionary wedge at the transition from subduction to mountain-building in Taiwan. *Earth and Planetary Science Letters*, *375*, 430–440. https://doi.org/10.1016/j.epsl.2013.06.007

Lock, J., & Willett, S. (2008). Low-temperature thermochronometric ages in fold-and-thrust belts. *Tectonophysics*, *456*(3–4), 147–162. https://doi.org/10.1016/j.tecto.2008.03.007

Madanipour, S., Ehlers, T. A., Yassaghi, A., & Enkelmann, E. (2017). Accelerated middle Miocene exhumation of the Talesh Mountains constrained by U-Th/He thermochronometry: Evidence for the Arabia-Eurasia collision in the NW Iranian Plateau: Cenozoic Exhumation of Talesh Mountains. *Tectonics*, *36*(8), 1538–1561. https://doi.org/10.1002/2016TC004291

McQuarrie, N., Stock, J. M., Verdel, C., & Wernicke, B. P. (2003). Cenozoic evolution of Neotethys and implications for the causes of plate motions. *Geophysical Research Letters*, *30*(20), doi:10.1029/2003GL017992-doi:10.1029/2003GL017992.

van der Meer, D. G., van Hinsbergen, D. J. J., & Spakman, W. (2018). Atlas of the underworld: Slab remnants in the mantle, their sinking history, and a new outlook on lower mantle viscosity. *Tectonophysics*, *723*, 309–448. https://doi.org/10.1016/j.tecto.2017.10.004

Mellors, R. J., Jackson, J., Myers, S. C., Gok, R., Priestly, K., Yetirmishli, G., et al. (2012). Deep earthquakes beneath the Northern Caucasus: Evidence of active or recent subduction in western Asia. *Bulletin of the Seismological Society of America*, *102*(2), 862–866.

Memiş, C., Göğüş, O. H., Uluocak, E. Ş., Pysklywec, R., Keskin, M., Şengör, A. M. C., & Topuz, G. (2020). Long Wavelength Progressive Plateau Uplift in Eastern Anatolia Since 20 Ma: Implications for the Role of Slab Peel-Back and Break-Off. *Geochemistry, Geophysics, Geosystems*, *21*(2). https://doi.org/10.1029/2019GC008726

Michel, L., Ehlers, T. A., Glotzbach, C., Adams, B. A., & Stübner, K. (2018). Tectonic and glacial contributions to focused exhumation in the Olympic Mountains, Washington, USA. *Geology*, *46*(6). https://doi.org/10.1130/G39881.1

Mikhailov, V. O., Panina, L. V., Polino, R., Koronovsky, N. V., Kiseleva, E. A., Klavdieva, N. V., & Smolyaninova, E. I. (1999). Evolution of the North Caucasus foredeep: constraints based on the analysis of subsidence curves. *Tectonophysics*, *307*, 361–379.

Moore, M. A., & England, P. C. (2001). On the inference of denudation rates from cooling ages of minerals. *Earth and Planetary Science Letters*, *185*(3–4), 265–284. https://doi.org/10.1016/S0012-821X(00)00380-0

Mosar, J., Kangarli, T., Bochud, M., Glasmacher, U. A., Rast, A., Brunet, M.-F., & Sosson, M. (2010). Cenozoic-Recent tectonics and uplift in the Greater Caucasus: a perspective from Azerbaijan. In M. Sosson, N. Kaymakci, R. A. Stephenson, F. Bergerat, & V. I. Starostenko (Eds.), *Sedimentary Basin Tectonics from the Black Sea and Caucasus to the Arabian Platform* (Vol. 340, pp. 261–280). London: Geological Society.

Motavalli-Anbaran, S.-H., Zeyen, H., & Jamasb, A. (2016). 3D crustal and lithospheric model of the Arabia–Eurasia collision zone. *Journal of Asian Earth Sciences*, *122*, 158–167. https://doi.org/10.1016/j.jseaes.2016.03.012

Mouthereau, F. (2011). Timing of uplift in the Zagros belt/Iranian plateau and accommodation of late Cenozoic Arabia–Eurasia convergence. *Geological Magazine*, *148*(5–6), 726–738. https://doi.org/10.1017/S0016756811000306

Müller, R. D., Cannon, J., Qin, X., Watson, R. J., Gurnis, M., Williams, S., et al. (2018). GPlates: Building a Virtual Earth Through Deep Time. *Geochemistry, Geophysics, Geosystems*, *19*(7), 2243–2261. https://doi.org/10.1029/2018GC007584

Mumladze, T., Forte, A. M., Cowgill, E., Trexler, C. C., Niemi, N. A., Yikilmaz, M. B., & Kellogg, L. H. (2015). Subducted, detached, and torn slabs beneath the Greater Caucasus. *GeoResJ*, *5*, 36–46. https://doi.org/10.1016/j.grj.2014.09.004

Nemčok, M., Glonti, B., Yukler, A., & Marton, B. (2013). Development history of the foreland plate trapped between two converging orogens; Kura Valley, Georgia, case study. In M. Nemčok, A. Mora, & J. W. Cosgrove (Eds.), *Thick-Skin-Dominated Orogens: From Initial Inversion to Full Accretion* (Vol. 377). London: Geolgical Society. https://doi.org/10.1144/SP377.9

Ouimet, W. B., Whipple, K. X., & Granger, D. E. (2009). Beyond threshold hillslopes: Channel adjustment to base-level fall in tectonically active mountain ranges. *Geology*, *37*(7), 579–582.

Pfiffner, O. A., Ellis, S., & Beaumont, C. (2000). Collision tectonics in the Swiss Alps: Insights from geodynamic modeling. *Tectonics*, *19*(6), 1065–1094.

Philip, H., Cisternas, A., Gvishiani, A., & Gorshkov, A. (1989). The Caucasus: an actual example of the initial stages of continental collision. *Tectonophysics*, *161*, 1–21.

Regard, V., Bellier, O., Thomas, J.-C., Abbassi, M. R., Mercier, J., Shabanian, E., et al. (2004). Accomodation of Arabia-Eurasia covnergence in the Zagros-Makran tranfers zone, SE Iran: A transition between collision and subduction through a young deforming system. *Tectonics*, *23*, doi:10.1029/2003TC001599-doi:10.1029/2003TC001599.

Regard, V., Hatzfeld, D., Molinaro, M., Aubourg, C., Bayer, R., Bellier, O., et al. (2010). The transition between Makran subduction and the Zagros collision: recent advances in its structure and active deformation. *Geological Society, London, Special Publications*, *330*(1), 43–64. https://doi.org/10.1144/SP330.4

Reilinger, R., McClusky, S., Vernant, P., Lawrence, S., Ergintav, S., Cakmak, R., et al. (2006). GPS constraints on continental deformation in the Africa-Arabia-Eurasia continental collision zone and implications for the dynamics of plate interactions. *Journal of Geophysical Research*, *111*, doi:10.1029/2005JB004051-doi:10.1029/2005JB004051.

Reiners, P. W., & Brandon, M. T. (2006). Using thermochronology to understand orogenic evolution. *Annual Review of Earth and Planetary Sciences*, *34*, 419–466. https://doi.org/10.1146/annurev.earth.34.031405.125202

Reiners, P. W., Spell, T. L., Nicolescu, S., & Zanetti, K. A. (2004). Zircon (U-Th)/He thermochronometry: He diffusion and comparisons with 40Ar/39Ar dating. *Geochimica et Cosmochimica Acta*, *68*(8), 1857–1887.

Reyners, M., & Cowan, H. (1993). The transition from subduction to continental collision: crustal structure in the North Canterbury region, New Zealand. *Geophysical Journal International*, *115*(3), 1124–1136. https://doi.org/10.1111/j.1365-246X.1993.tb01514.x

Rezaeian, M., Carter, A., Hovius, N., & Allen, M. B. (2012). Cenozoic exhumation history of the Alborz Mountains, Iran: New constraints from low-temperature chronometry: CENOZOIC EPISODIC EXHUMATION. *Tectonics*, *31*(2), n/a-n/a. https://doi.org/10.1029/2011TC002974

Robert, A. M. M., Fernàndez, M., Jiménez-Munt, I., & Vergés, J. (2017). Lithospheric structure in Central Eurasia derived from elevation, geoid anomaly and thermal analysis. *Geological Society, London, Special Publications*, *427*(1), 271–293. https://doi.org/10.1144/SP427.10

Rohatgi, A. (2020). WebPlotDigitzier (Version 4.4). Retrieved from https://automeris.io/WebPlotDigitizer

Ruhl, K. W., & Hodges, K. V. (2005). The use of detrital mineral cooling ages to evaluate steady state assumptions in active orogens: An example from the central Nepalese Himalaya. *Tectonics*, *24*(TC4015). https://doi.org/10.1029/2004TC001712

Ruppel, C., & McNutt, M. (1990). Regional compensation of the Greater Caucasus mountains based on an analysis of Bouguer gravity data. *Earth and Planetary Science Letters*, *98*, 360–379.

Safran, E. B., Bierman, P. R., Aalto, R., Dunne, T., Whipple, K. X., & Caffee, M. W. (2005). Erosion rates driven by channel network incision in the Bolivian Andes. *Earth Surface Processes and Landforms*, *30*, 1007–1024.

Saintot, A., Brunet, M.-F., Yakovlev, F., Sebrier, M., Stephenson, R. A., Ershov, A. V., et al. (2006). The Mesozoic-Cenozoic tectonic evolution of the Greater Caucasus. In D. G. Gee & R. A. Stephenson (Eds.), *European Lithosphere Dynamics* (Vol. 32). London: Geological Society.

Şengör, A. M. C. (1984). The Cimmeride Orogenic System and the Tectonics of Eurasia. *Geological Society of America Special Paper*, *195*, 1–82.

Seton, M., Müller, R. D., Zahirovic, S., Gaina, C., Torsvik, T., Shephard, G., et al. (2012). Global continental and ocean basin reconstructions since 200Ma. *Earth-Science Reviews*, *113*(3–4), 212–270. https://doi.org/10.1016/j.earscirev.2012.03.002

Shengelaya, G. S. (1984). *Gravity model of the earth crust of the Caucasus*. Moscow: Nauka.

Skolbeltsyn, G., Mellors, R., Gök, R., Türkelli, N., Yetirmishli, G., & Sandvol, E. (2014). Upper mantle S wave velocity structure of the East Anatolian-Caucasus region. *Tectonics*, *33*, 207–221. https://doi.org/10.1002/2013TC003334

Sobornov, K. O. (1994). Structure and petroleum potential of the Dagestan thrust belt, northeastern Caucasus, Russia. *Bulletin of Canadian Petroleum Geology*, *42*(3), 352–364.

Sobornov, K. O. (1996). Lateral variations in structural styles of tectonic wedging in the northeastern Caucasus. *Bulletin of Canadian Petroleum Geology*, *44*(2), 385–399.

Sokhadze, G., Floyd, M., Godoladze, T., King, R., Cowgill, E. S., Javakhishvili, Z., et al. (2018). Active convergence between the Lesser and Greater Caucasus in Georgia: Constraints on the tectonic evolution of the Lesser–Greater Caucasus continental collision. *Earth and Planetary Science Letters*, *481*, 154–161. https://doi.org/10.1016/j.epsl.2017.10.007

Somin, M. L. (2011). Pre-Jurassic Basement of the Greater Caucasus: Brief Overview. *Turkish Journal of Earth Sciences*, *20*, 546–610.

Stock, G. M., Ehlers, T. A., & Farley, K. A. (2006). Where does sediment come from? Quantifying catchment erosion with detrital apatite (U-Th)/He thermochronometry. *Geology*, *34*(9), 725–728.

Stockli, D. F., Farley, K. A., & Dumitru, T. (2000). Calibration of the apatite (U-Th)/He thermochronometer on an exhumed fault block, White Mountains, California. *Geology*, *28*(11), 983–986.

Sukhishvili, L., Forte, A. M., Merebashvili, G., Leonard, J., Whipple, K. X., Javakhishvili, Z., et al. (2020). Active deformation and Plio-Pleistocene fluvial reorganization of the western Kura fold–thrust belt, Georgia: implications for the evolution of the Greater Caucasus Mountains. *Geological Magazine*, 1–15. https://doi.org/10.1017/S0016756820000709

Tate, G. W., McQuarrie, N., Van Hinsbergen, D. J. J., Bakker, R. R., Harris, R., & Jiang, H. (2015). Australia going down under: Quantifying continental subduction during arc-continent accretion in Timor-Leste. *Geosphere*, *11*(6), 1860–1883. https://doi.org/10.1130/GES01144.1

Trexler, C. C., Cowgill, E., Spencer, J. Q. G., & Godoladze, T. (2020). Rate of active shortening across the southern thrust front of the Greater Caucasus in western Georgia from kinematic modeling of folded river terraces above a listric thrust. *Earth and Planetary Science Letters*, *544*, 116362. https://doi.org/10.1016/j.epsl.2020.116362

Trexler, C. C., Cowgill, E. S., Niemi, N. A., Vasey, D. A., & Godoladze, T. (2022). Tectonostratigraphy and major structures of the Georgian Greater Caucasus: Implications for structural architecture, along-strike continuity, and orogen evolution. *Geosphere*. https://doi.org/10.1130/GES02385.1

Tripathy-Lang, A., Hodges, K. V., Monteleone, B. D., & Van Soest, M. C. (2013). Laser (U-Th)/He thermochronology of detrital zircons as a tool for studying surface processes in modern catchments. *Journal of Geophysical Research: Earth Surface*, *118*(3), 1333–1341. https://doi.org/10.1002/jgrf.20091

Tsereteli, N., Tibaldi, A., Alania, V., Gventsadse, A., Enukidze, O., Varazanashvili, O., & Müller, B. I. R. (2016). Active tectonics of central-western Caucasus, Georgia. *Tectonophysics*, *691*, 328–344. https://doi.org/10.1016/j.tecto.2016.10.025

Tye, A. R. (2019). *Continental Deformation: New Tools and New Constraints on Convergent and Collisional Tectonic Systems from the Greater Caucasus* (PhD). University of Michigan.

Tye, A. R., Niemi, N. A., Safarov, R. T., Kadirov, F. A., & Babayev, G. R. (2020). Sedimentary response to a collision orogeny recorded in detrital zircon provenance of Greater

Caucasus foreland basin sediments. *Basin Research*, bre.12499. https://doi.org/10.1111/bre.12499

Vanderhaeghe, O. (2012). The thermal-mechanical evolution of crustal orogenic belts at convergent plate boundaries: A reappraisal of the orogenic cycle. *Journal of Geodynamics*, *56–57*, 124–145.

Vanderhaeghe, O., & Duchene, S. (2010). Crustal-scale mass transfer, geotherm and topography at convergent plate boudaries. *Terra Nova*, *22*, 315–323.

Vasey, D. A., Cowgill, E., Roeske, S. M., Niemi, N. A., Godoladze, T., Skhirtladze, I., & Gogoladze, S. (2020). Evolution of the Greater Caucasus Basement and Formation of the Main Caucasus Thrust, Georgia. *Tectonics*, *39*(3). https://doi.org/10.1029/2019TC005828

Vermeesch, P. (2004). How many grains are needed for a provenance study? *Earth and Planetary Science Letters*, *224*, 441–451.

Vermeesch, P. (2012). On the visualization of detrital age distributions. *Chemical Geology*, *312–313*, 190–194.

Vermeesch, P., Sherlock, S. C., Roberts, N. M. W., & Carter, A. (2012). A simple method for in-situ U–Th–He dating. *Geochimica et Cosmochimica Acta*, *79*, 140–147. https://doi.org/10.1016/j.gca.2011.11.042

Vezzoli, G., Garzanti, E., Vincent, S. J., Ando, S., Carter, A., & Resentini, A. (2014). Tracking sediment provenance and erosional evolution of the western Greater Caucasus. *Earth Surface Processes and Landforms*. https://doi.org/10.1002/esp.3567

Vezzoli, G., Garzanti, E., Limonta, M., & Radeff, G. (2020). Focused erosion at the core of the Greater Caucasus: Sediment generation and dispersal from Mt. Elbrus to the Caspian Sea. *Earth-Science Reviews*, *200*, 102987. https://doi.org/10.1016/j.earscirev.2019.102987

Vincent, S. J., Morton, A. C., Carter, A., Gibbs, S., & Teimuraz, G. B. (2007). Oligocene uplift of the Western Greater Caucasus: an effect of initial Arabia-Eurasia collision. *Terra Nova*, *19*, 160–166.

Vincent, S. J., Carter, A., Lavrishchev, A., Rice, S. P., Barabadze, T. G., & Hovius, N. (2011). The exhumation of the western Greater Caucasus: a thermochronometric study. *Geological Magazine*, *148*, 1–21. https://doi.org/10.1017/S0016756810000257

Vincent, S. J., Braham, W., Lavrishchev, V. A., Maynard, J. R., & Harland, M. (2016). The formation and inversion of the western Greater Caucasus Basin and the uplift of the western Greater Caucasus: Implications for the wider Black Sea region. *Tectonics*, *35*(12), 2948–2962. https://doi.org/10.1002/2016TC004204

Vincent, S. J., Saintot, A., Mosar, J., Okay, A. I., & Nikishin, A. M. (2018). Comment on “Relict basin closure and crustal shortening budgets during continental collision: An example from Caucasus sediment provenance” by Cowgill et al (2016). *Tectonics*, *37*, 1006–1016. https://doi.org/10.1002/2017TC004515

Vincent, S. J., Somin, M. L., Carter, A., Vezzoli, G., Fox, M., & Vautravers, B. (2020). Testing Models of Cenozoic Exhumation in the Western Greater Caucasus. *Tectonics*, *39*(2). https://doi.org/10.1029/2018TC005451

Whipple, K. X. (2001). Fluvial landscape response time: How plausible is steady-state denudation? *American Journal of Science*, *301*, 313–325.

Whipple, K. X., & Meade, B. (2004). Controls on the strength of coupling among climate, erosion, and deformation in two-sided, frictional orogenic wedges at steady state. *Journal of Geophysical Research*, *109*, F01011–F01011. https://doi.org/10.1029/2003JF000019

Whipple, K. X., & Tucker, G. E. (1999). Dynamics of the stream-power river incision model: Implications for height limits of mountain ranges, landscape response timescales, and research needs. *Journal of Geophysical Research*, *104*(B8), 17661–17674.

Willett, S. D., & Brandon, M. T. (2013). Some analytical methods for converting thermochronometric age to erosion rate: AGE TO EROSION RATE. *Geochemistry, Geophysics, Geosystems*, *14*(1), 209–222. https://doi.org/10.1029/2012GC004279

Willett, S. D., Beaumont, C., & Fullsack, P. (1993). Mechanical model for the tectonics of doubly vergent compressional orogens. *Geology*, *21*, 371–374.

Willett, S. D., Slingerland, R. L., & Hovius, N. (2001). Uplift, shortening, and steady state topography in active mountain belts. *American Journal of Science*, *301*, 455–485.

Wolf, R. A., Farley, K. A., & Kass, D. M. (1998). Modeling of the temperature sensitivity of the apatite (U-Th)/He thermochronometer. *Chemical Geology*, *148*, 105–114.

Zonenshain, L. P., & Le Pichon, X. (1986). Deep basins of the Black Sea and Caspian Sea as remnants of Mesozoic back-arc basins. *Tectonophysics*, *123*, 181–211.

Zor, E. (2008). Tomographic evidence of slab detachment beneath eastern Turkey and the Caucasus. *Geophysical Journal International*, *175*, 1273–1282.

Figure 1.

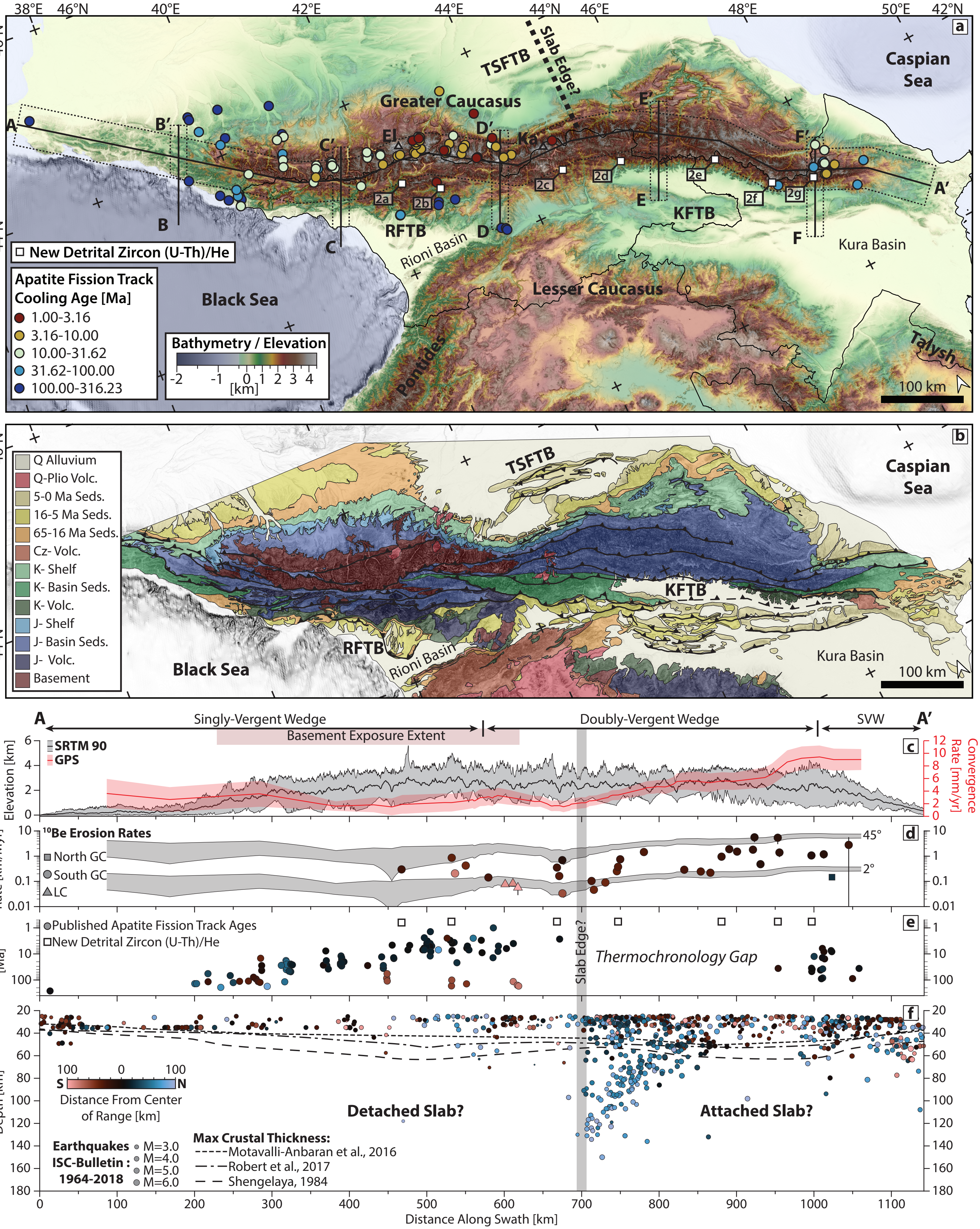

a
TSFTB
Slab Edge?
Greater Caucasus
Caspian Sea
A
B′
B
C′
C
EI
D′
D
Ka
E′
E
F′
F
A′
2a
2b
2c
2d
2e
2f
2g
RFTB
KFTB
Rioni Basin
Kura Basin
Black Sea
Lesser Caucasus
Pontides
Talysh
New Detrital Zircon (U-Th)/He
Apatite Fission Track Cooling Age [Ma]
1.00-3.16
3.16-10.00
10.00-31.62
31.62-100.00
100.00-316.23
Bathymetry / Elevation
-2 -1 0 1 2 3 4
[km]
100 km
b
Q Alluvium
Q-Plio Volc.
5-0 Ma Seds.
16-5 Ma Seds.
65-16 Ma Seds.
Cz- Volc.
K- Shelf
K- Basin Seds.
K- Volc.
J- Shelf
J- Basin Seds.
J- Volc.
Basement
TSFTB
Caspian Sea
KFTB
RFTB
Rioni Basin
Kura Basin
Black Sea
100 km
Singly-Vergent Wedge
Doubly-Vergent Wedge
SVW
Basement Exposure Extent
c
SRTM 90
GPS
Elevation [km]
Convergence Rate [mm/yr]
d
^{10}Be Erosion Rates
North GC
South GC
LC
Erosion/Uplift Rate [km/Myr]
45°
2°
e
Published Apatite Fission Track Ages
New Detrital Zircon (U-Th)/He
Cooling Age [Ma]
Slab Edge?
Thermochronology Gap
f
Depth [km]
Distance From Center of Range [km]
S
N
Detached Slab?
Attached Slab?
Earthquakes ISC-Bulletin : 1964-2018
M=3.0
M=4.0
M=5.0
M=6.0
Max Crustal Thickness:
Motavalli-Anbaran et al., 2016
Robert et al., 2017
Shengelaya, 1984
Distance Along Swath [km]

Figure 2.

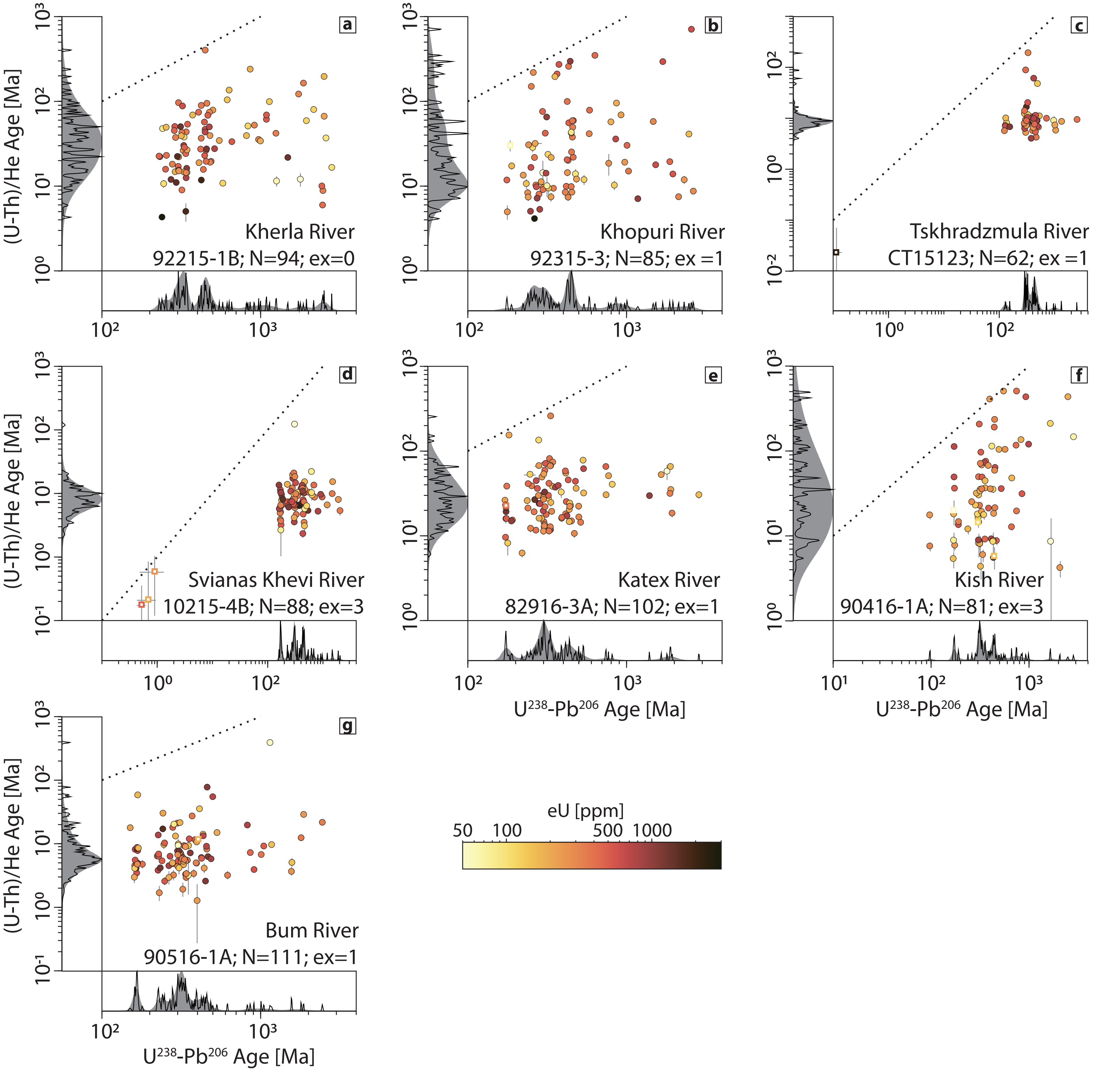

(U-Th)/He Age [Ma]
U238-Pb206 Age [Ma]
a
Kherla River
92215-1B; N=94; ex=0
b
Khopuri River
92315-3; N=85; ex =1
c
Tskhradzmula River
CT15123; N=62; ex =1
d
Svianas Khevi River
10215-4B; N=88; ex=3
e
Katex River
82916-3A; N=102; ex=1
f
Kish River
90416-1A; N=81; ex=3
g
Bum River
90516-1A; N=111; ex=1
eU [ppm]
50 100 500 1000

Figure 3.

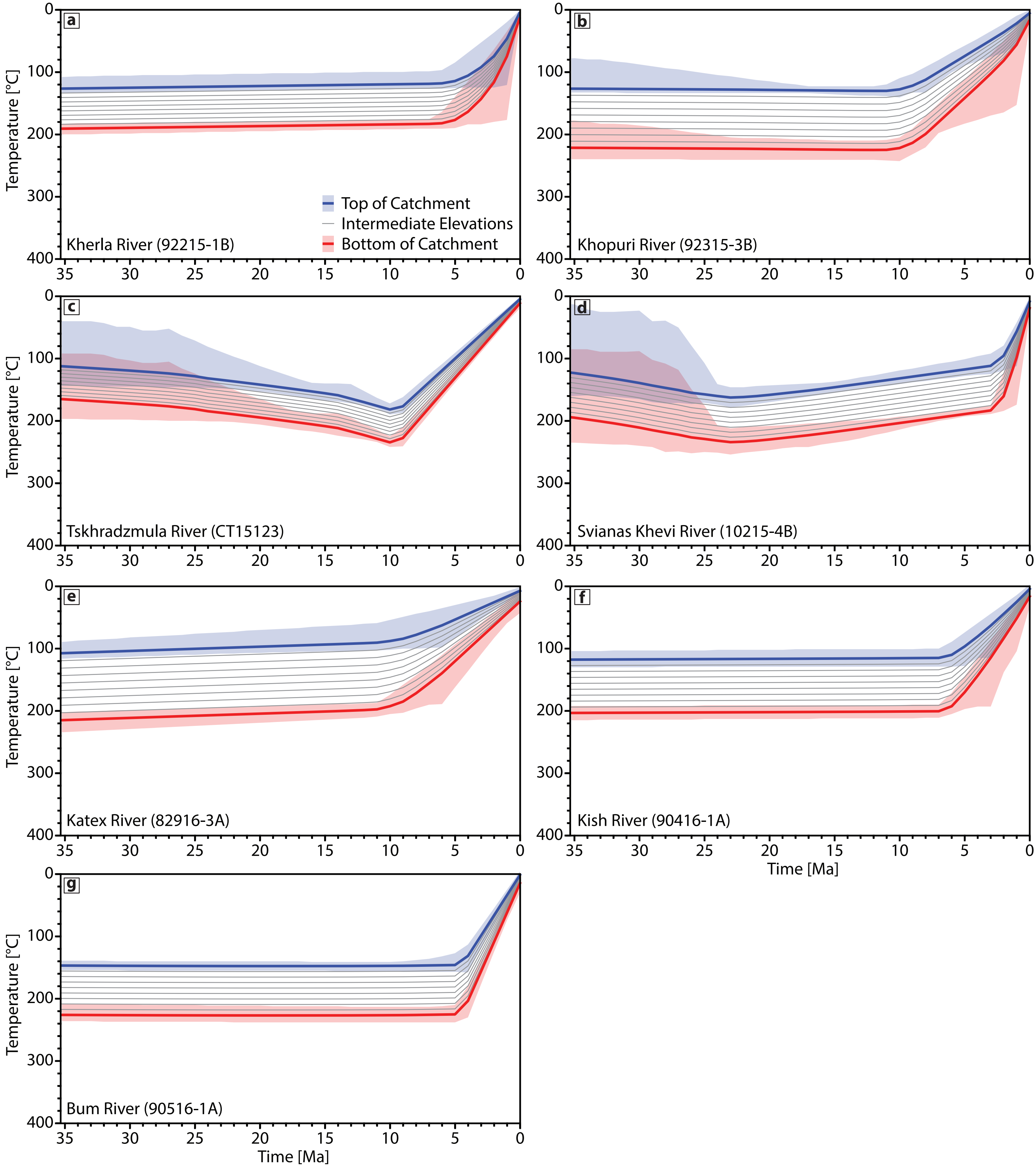

a
Kherla River (92215-1B)
Top of Catchment
Intermediate Elevations
Bottom of Catchment
b
Khopuri River (92315-3B)
c
Tskhradzmula River (CT15123)
d
Svianas Khevi River (10215-4B)
e
Katex River (82916-3A)
f
Kish River (90416-1A)
g
Bum River (90516-1A)
Temperature [°C]
Time [Ma]
0
100
200
300
400
35
30
25
20
15
10
5
0

Figure 4.

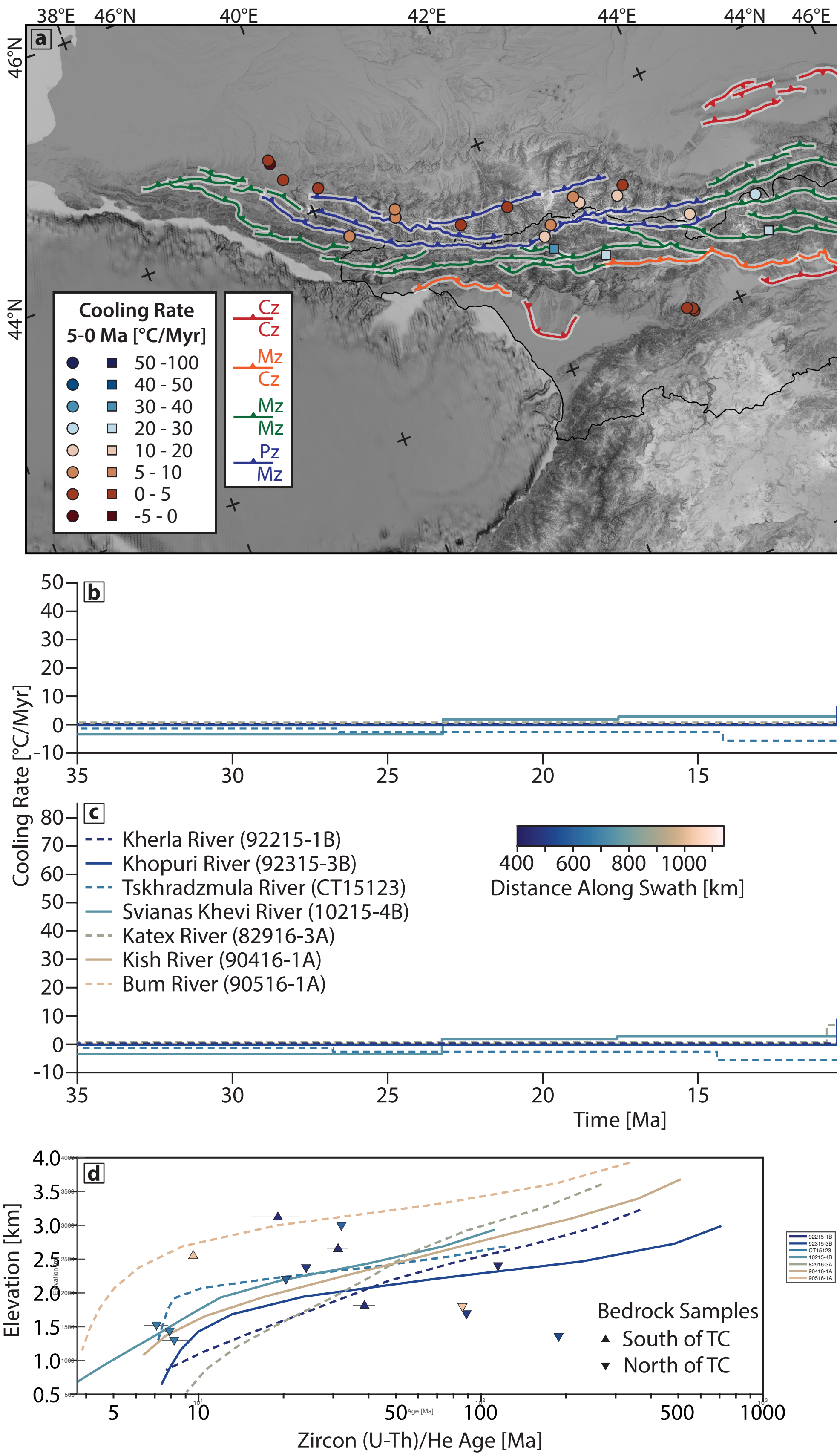
a
38°E
46°N
40°E
42°E
44°E
44°N
46°E
48°E
50°E
42°N
Cooling Rate
5-0 Ma [°C/Myr]
50 -100
40 - 50
30 - 40
20 - 30
10 - 20
5 - 10
0 - 5
-5 - 0
Cz
Cz
Mz
Cz
Mz
Mz
Pz
Mz
100 km
b
Cooling Rate [°C/Myr]
Exhumation Rate - 40°C/km [km/Myr]
Exhumation Rate - 20°C/km [km/Myr]
c
Kherla River (92215-1B)
Khopuri River (92315-3B)
Tskhradzmula River (CT15123)
Svianas Khevi River (10215-4B)
Katex River (82916-3A)
Kish River (90416-1A)
Bum River (90516-1A)
Distance Along Swath [km]
Time [Ma]
d
Elevation [km]
Bedrock Samples
South of TC
North of TC
Zircon (U-Th)/He Age [Ma]

Figure 5.

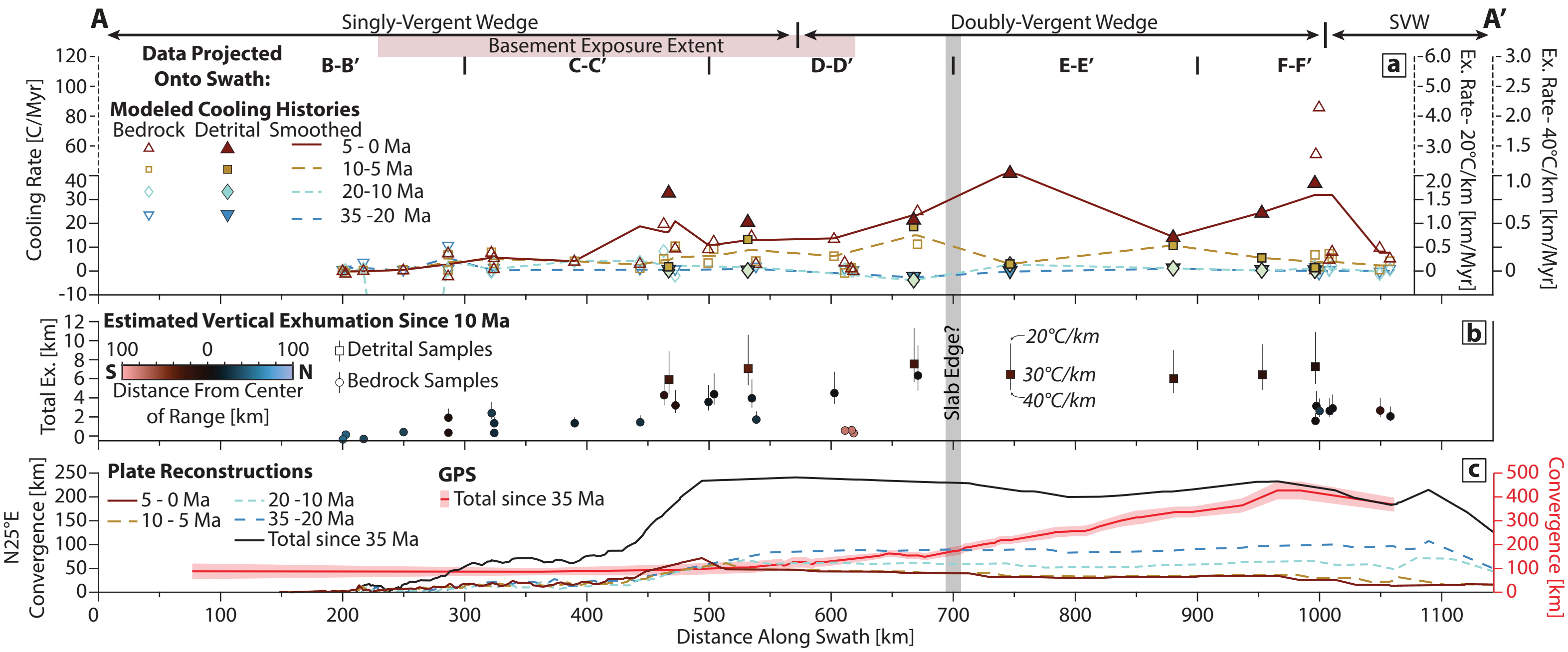

A
A′
Singly-Vergent Wedge
Doubly-Vergent Wedge
SVW
Basement Exposure Extent
B-B′
C-C′
D-D′
E-E′
F-F′
a
Data Projected Onto Swath:
Modeled Cooling Histories
Bedrock Detrital Smoothed
5 - 0 Ma
10-5 Ma
20-10 Ma
35 -20 Ma
Cooling Rate [C/Myr]
Ex. Rate- 20°C/km [km/Myr]
Ex. Rate- 40°C/km [km/Myr]
b
Estimated Vertical Exhumation Since 10 Ma
Total Ex. [km]
S
N
Distance From Center of Range [km]
Detrital Samples
Bedrock Samples
Slab Edge?
20°C/km
30°C/km
40°C/km
c
Plate Reconstructions
5 - 0 Ma
10 - 5 Ma
20 -10 Ma
35 -20 Ma
Total since 35 Ma
GPS
Total since 35 Ma
N25°E Convergence [km]
Distance Along Swath [km]

Figure 6.

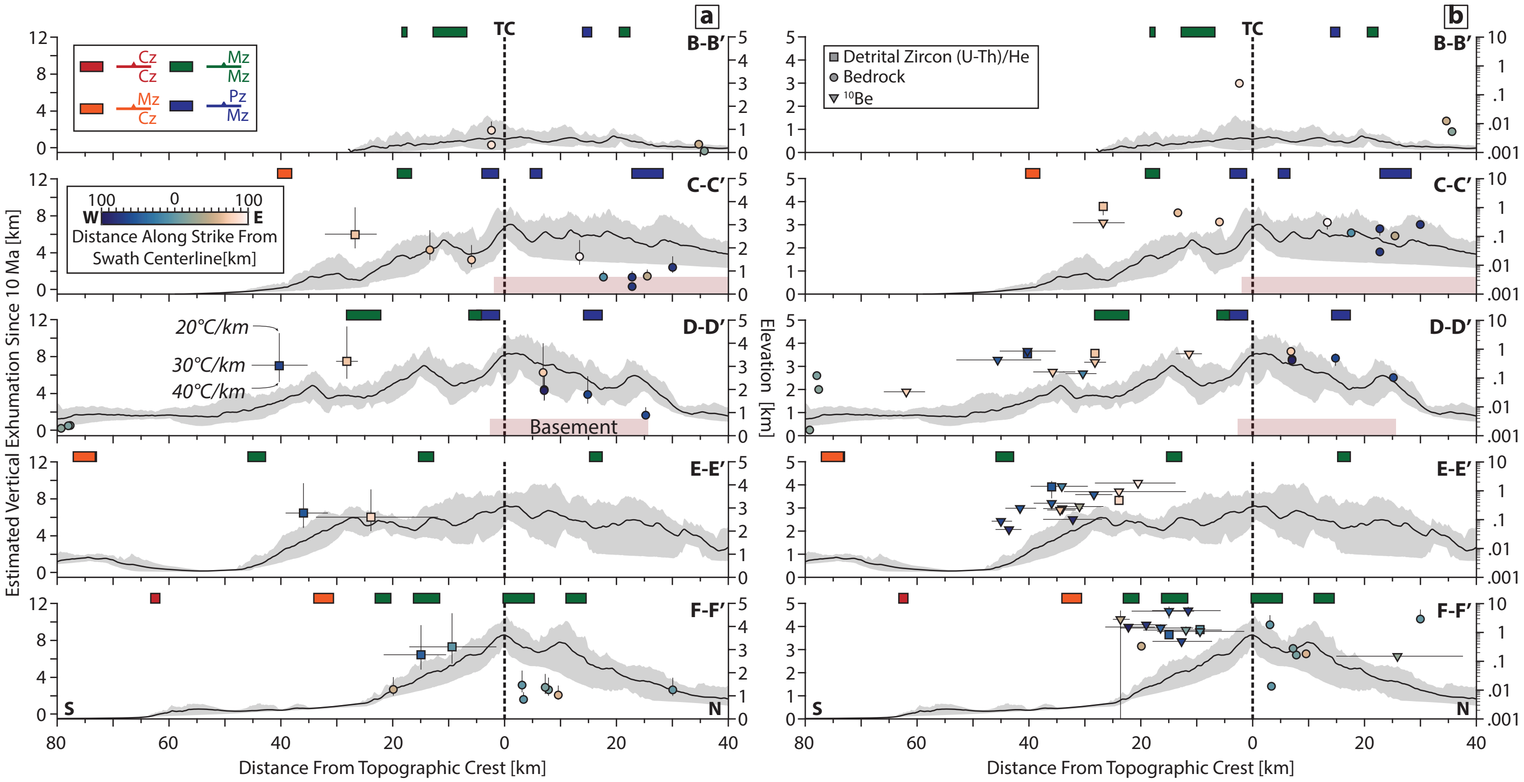
a
b
TC
B-B′
C-C′
D-D′
E-E′
F-F′
Cz
Mz
Pz
100
0
100
W
E
Distance Along Strike From Swath Centerline[km]
20°C/km
30°C/km
40°C/km
Basement
Estimated Vertical Exhumation Since 10 Ma [km]
Elevation [km]
Exhumation Rate [km/Ma]
Detrital Zircon (U-Th)/He
Bedrock
^{10}Be
S
N
Distance From Topographic Crest [km]

Figure 7.

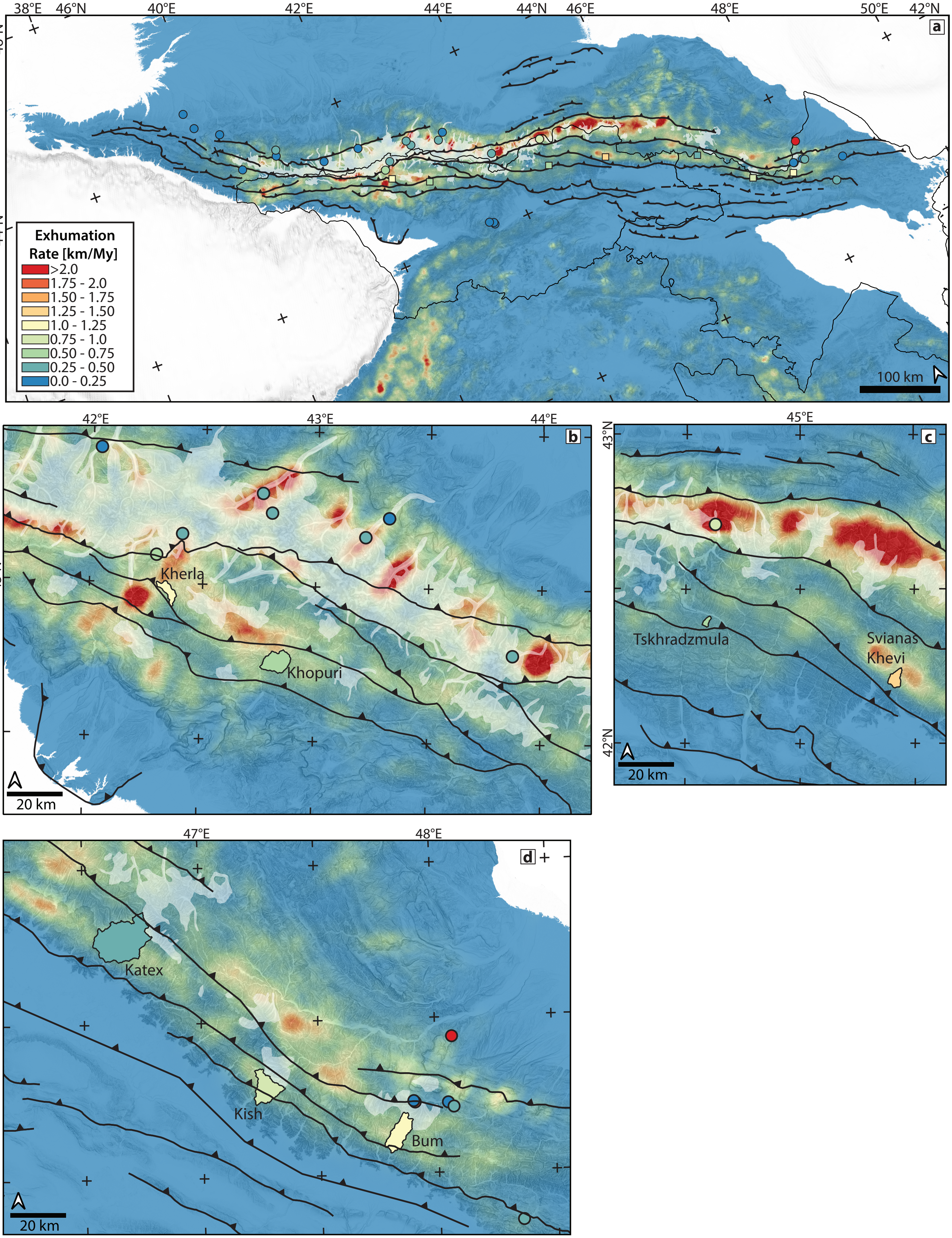
a
38°E
46°N
40°E
42°E
44°E
44°N
46°E
48°E
50°E
42°N
46°N
44°N
Exhumation
Rate [km/My]
>2.0
1.75 - 2.0
1.50 - 1.75
1.25 - 1.50
1.0 - 1.25
0.75 - 1.0
0.50 - 0.75
0.25 - 0.50
0.0 - 0.25
100 km
b
42°E
43°E
44°E
43°N
Kherla
Khopuri
20 km
c
45°E
43°N
42°N
Tskhradzmula
Svianas
Khevi
20 km
d
47°E
48°E
42°N
41°N
Katex
Kish
Bum
20 km

Figure 8.

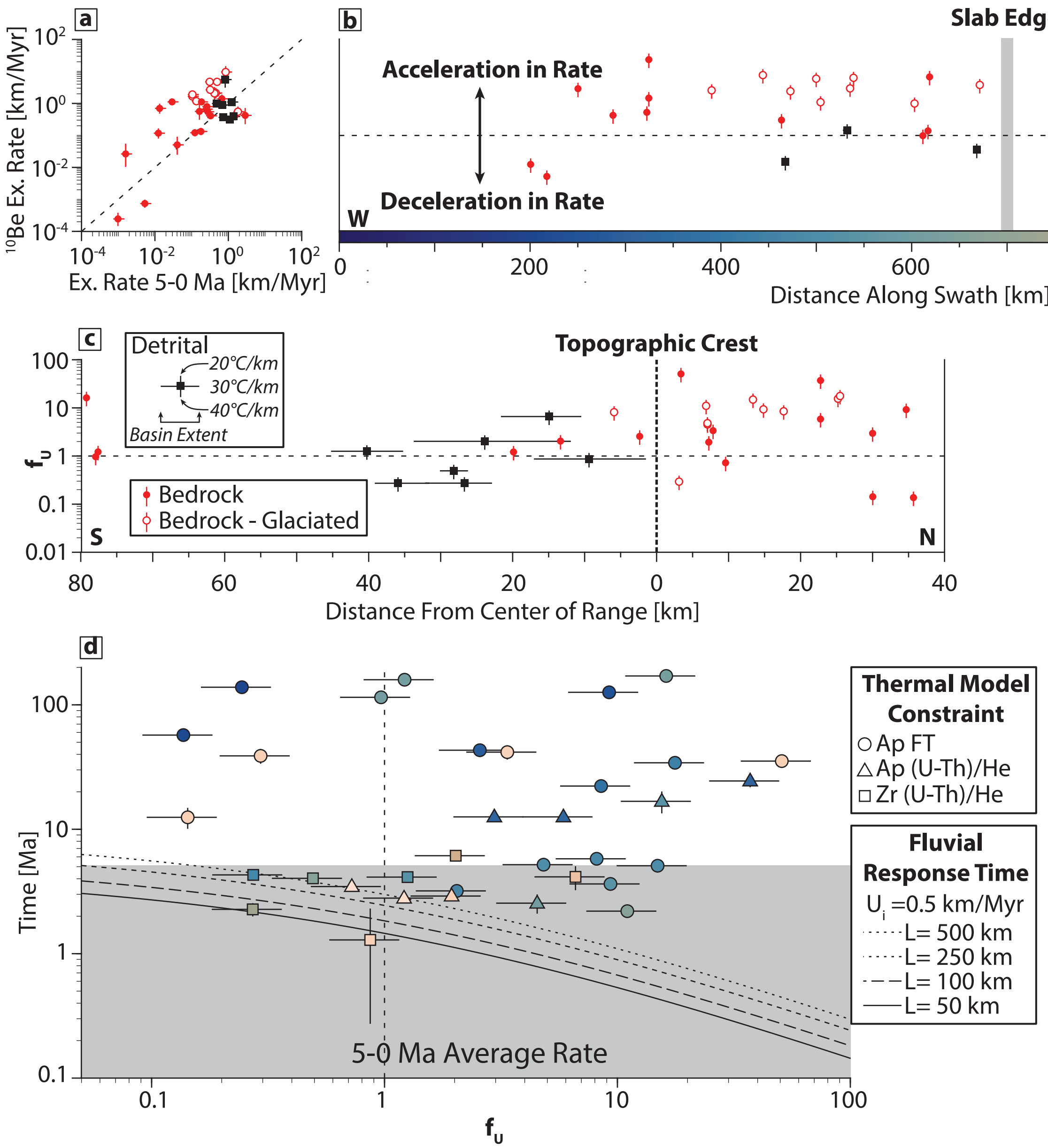
a
^{10}Be Ex. Rate [km/Myr]
Ex. Rate 5-0 Ma [km/Myr]
b
Slab Edge?
Acceleration in Rate
Deceleration in Rate
W
E
Distance Along Swath [km]
f_u
c
Detrital
20°C/km
30°C/km
40°C/km
Basin Extent
Topographic Crest
Bedrock
Bedrock - Glaciated
S
N
Distance From Center of Range [km]
d
Thermal Model Constraint
Ap FT
Ap (U-Th)/He
Zr (U-Th)/He
Fluvial Response Time
U_i =0.5 km/Myr
L= 500 km
L= 250 km
L= 100 km
L= 50 km
5-0 Ma Average Rate
Time [Ma]
f_u

Figure 9.

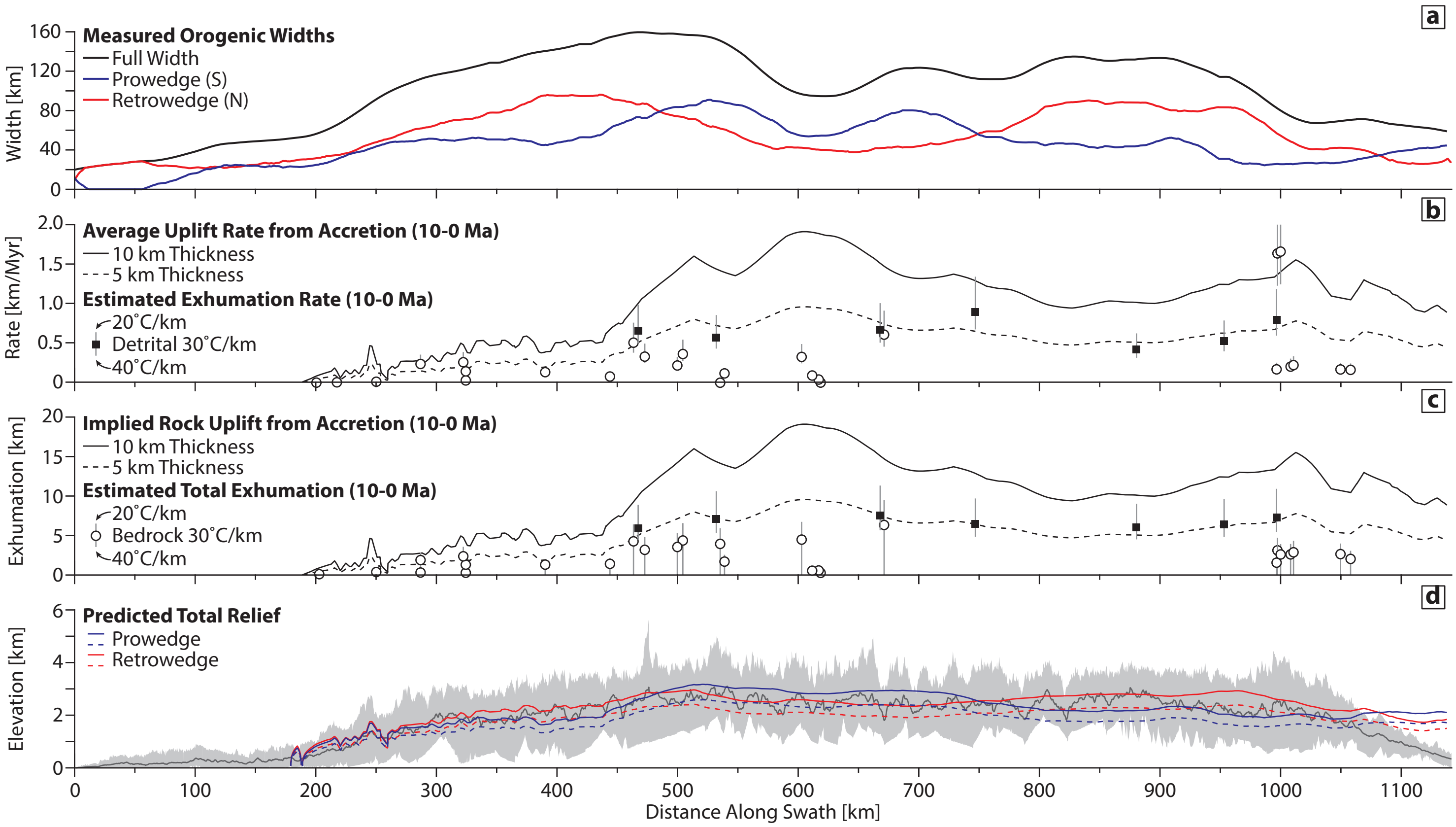
a
Measured Orogenic Widths
Full Width
Prowedge (S)
Retrowedge (N)
Width [km]
b
Average Uplift Rate from Accretion (10-0 Ma)
10 km Thickness
5 km Thickness
Estimated Exhumation Rate (10-0 Ma)
20°C/km
Detrital 30°C/km
40°C/km
Rate [km/Myr]
c
Implied Rock Uplift from Accretion (10-0 Ma)
10 km Thickness
5 km Thickness
Estimated Total Exhumation (10-0 Ma)
20°C/km
Bedrock 30°C/km
40°C/km
Exhumation [km]
d
Predicted Total Relief
Prowedge
Retrowedge
Elevation [km]
Distance Along Swath [km]